CALIBRATION-BASED REGULARIZATION FOR SPECTRAL IMAGE RECOVERY IN OPTIMIZED CODIFIED ACQUISITION SYSTEMS

Hans Yecid Garcia Arenas

Magister en ingeniería electrónica

Universidad Industrial de Santander

Facultad de Ingenierías Fisicomecánicas

Escuela de Ingenierías Eléctrica, Electrónica y de Telecomunicaciones

Bucaramanga

2023

CALIBRATION-BASED REGULARIZATION FOR SPECTRAL IMAGE RECOVERY IN OPTIMIZED CODIFIED ACQUISITION SYSTEMS

Hans Yecid Garcia Arenas

Magister en ingeniería electrónica

Doctoral thesis to qualify for the title of *Doctor en ingeniería, área ingniería electrónica*

Advisor

Henry Arguello Fuentes

Ph.D. Electrical and Computer Engineering

Universidad Industrial de Santander

Universidad Industrial de Santander

Facultad de Ingenierías Fisicomecánicas

Escuela de Ingenierías Eléctrica, Electrónica y de Telecomunicaciones

Bucaramanga

2023

Contents

List of Figures

Resumen

Titulo: Regularización basada en calibración para la recuperación de imágenes espectrales en sistemas de adquisición codificada optimizados.

Director: Ph.D. Henry Arguello Fuentes, henarfu@uis.edu.co.

Autor: Hans Garcia Arenas, hans.garcia@correo.uis.edu.co.

Entidad: Universidad Industrial de Santander.

Interesado: High Dimensional Signal Processing Group (HDSP).

Los sistemas de adquisición codificada son fundamentales en la captura de imágenes espectrales computacionales para adquirir escenas codificadas, las cuales son recuperadas resolviendo un problema inverso. El diseño de adquisición codificada es crucial al determinar las propiedades de invertibilidad de la matriz de detección del sistema. Para garantizar un diseño realista, el modelo de adquisición modelado matemáticamente debe coincidir con el sistema fisico. Sin embargo, existen variaciones estocásticas relacionadas con características no ideales de la implementación, además, dado que estas variaciones no se conocen previamente deben ser calibradas en el laboratorio. Por lo tanto, el diseño de codificación conduce a un rendimiento subóptimo en la práctica, incluso si se lleva a cabo un proceso de calibración exhaustivo. Esta tesis desarrolla una comprensión profunda de cómo el desajuste de calibración afecta el rendimiento de recuperación y proponen tres enfoques para reducir su efecto en algoritmos de reconstrucción de sistemas de imágenes espectrales codificados optimizados. Específicamente, se proponen dos regularizadores que aceleran la convergencia a través de las iteraciones del algoritmo de gradiente decendiente del sistema calibrado real, en la dirección del sistema originalmente optimizado teóricamente, y un enfoque más que estima las medidas ideales a partir de las medidas reales calibradas, empleando un enfoque de aprendizaje profundo para aumentar el rendimiento de la reconstrucción.

Abstract

Title: Calibration-based Regularization for Spectral Image Recovery in Optimized Codified Acquisition Systems.

Director: Ph.D. Henry Arguello Fuentes, henarfu@uis.edu.co.

Author: Hans Garcia Arenas, hans.garcia@correo.uis.edu.co.

Entity: Universidad Industrial de Santander.

Stakeholder: High Dimensional Signal Processing Group (HDSP).

Codified acquisition systems are a fundamental tool in snapshot computational spectral imaging for capturing encoded scenes that are then recovered by solving an inverse problem. Codified acquisition design is crucial, as it determines the invertibility properties of the system sensing matrix. To ensure a realistic design, the optical mathematical forward model must match the physical sensing. However, there exist stochastic variations related to non-ideal characteristics of the implementation; therefore, these variables are not known a priori and have to be calibrated in the laboratory setup. Thus, the optical encoding design leads to suboptimal performance in practice, even if an exhaustive calibration process is carried out. This thesis develops a deep understanding of how the calibration mismatch affects the recovery performance and proposes three approaches to reduce the effect in optimized codified spectral imaging systems reconstruction algorithms. Specifically, two regularizers are proposed that perform the gradient algorithm iterations of the real calibrated system in the direction of the originally theoretically optimized system, and an extension approach that estimates the ideal measurements from the real measurements using a deep learning approach to increase the reconstruction performance in terms of PSNR, SSIM, and SAM metrics.

Introduction

Codified acquisition systems, which map an underlying spectral image into 2D projections, are fundamental tools in snapshot computational spectral imaging (CSI), allowing spectral image reconstruction Arce et al. (2014); Bacca et al. (2021). Some CSI systems can be modeled as linear systems, i.e., the measurements $\mathbf{y}_0$ can be calculated as $\mathbf{y}_0 = \mathbf{H}_0\mathbf{x} + \mathbf{w}$, where $\mathbf{H}_0$ is the sensing matrix, $\mathbf{x}$ is the spectral image, and $\mathbf{w}$ represents the system noise. The sensing matrix $\mathbf{H}_0$ models the linear interaction between the scene and the optical elements such as coding elements, prisms, gratings, and other elements that contain the optical system. This work focuses on the entries of $\mathbf{H}_0$ that model the free parameters of the encoding, which can be implemented by elements such as digital micro-mirror-devices (DMD) Bacca et al. (2020), transmissive-based elements Arce et al. (2014), and diffractive optical elements (DOE) Arguello et al. (2021). The proposed methods are based on the fact that the designed elements of the sensing matrix $\mathbf{H}_0$ are implemented in the optical system and the exactly calibrated sensing matrix $\mathbf{H}_1 = \mathbf{H}_0 + \mathbf{H}_2$, the designed sensing matrix $\mathbf{H}_0$, and the mismatch matrix $\mathbf{H}_2$ are known. Under this decomposition, to analyze the effect of the $\mathbf{H}_2$ in the inverse problem solution, a gradient descent-based analysis is carried out, specifically, the gradient of the baseline ℓ_2 loss function is composed by the designed gradient direction, which depends on $\mathbf{H}_0$ and two extra terms that represent a deviation from the designed model in the implementation process. Therefore, this work proposes three approaches to mitigate the loss of performance in calibrated snapshot spectral imaging problems, caused by the unknown mismatch between the real model and the designed one, two of them are based on the inclusion of reinforcement regularization terms in the recovery problem in spectral imaging and the last one includes a pre-processing step based on deep learning to correct the real measurements $\mathbf{y}_1$ in the direction of the desired $\mathbf{y}_0$.

1. Objectives

General

- To design regularization terms based on calibration matrices to improve the reconstruction quality of optimized codified spectral imaging systems.

Specifics

- To determine the impact of the calibration in the sensing matrix and the recovery algorithm of optimized codified spectral imaging systems.
- To design a regularization based on the calibration to improve the quality of the recovered spectral images.
- To implement in the optical laboratory at least two optimized codified spectral imaging systems and to estimate the corresponding calibration terms.
- To verify the performance of the designed correction terms for the real optimized measurements and for at least two recovery approaches.

Impact of the Research and Contributions

This research thesis will address the problems introduced in chapters 3 and 4, which are related to the reduction of performance given by the non-ideal implementation, in a recovery task for spectral images, in optimized codified acquisition systems. Two approaches to deal with the mentioned problems are presented: first, an strategy that includes a regularization in the cost function to develop the recovery step, and second an strategy that employs a deep learning technique to mitigate the mismatch of the measurements acquired in the calibration stage with the designed measurements. Specifically, the main contributions of this thesis given by chapters are:

Chapter 3 Optimized codified system design analysis: In this chapter, an analysis of the performance of the reconstruction task obtained by the state-of-the-art codified spectral imaging systems is presented, also a comparison is carried out in terms of the eigenvalues of linear modeled systems using the theoretically designed sensing matrix compared with a calibrated matrix.

Chapter 4 Impact of calibration: In this chapter, using the analysis developed in chapter 3 is determined the impact of the calibration in the sensing matrix from the performance of the recovery algorithm, assuming an additive model of distortion in the implementation, also, some examples trying to estimate the distortion are presented, assuming convolution kernels in order to illustrate the mismatch model complexity before the implementation. This chapter presents the process to obtain the calibrated matrix from DOE-based and the CASSI optical systems in a test-bed implementation developed in the HDSP group laboratory, remarking that both systems are employed to acquire spectral images based on compressive sensing theory.

Chapter 5 Calibration Reinforcement Regularizations for Optimized Snapshot Spectral Imaging: In this chapter, a mathematical analysis of the effect caused by the calibration of the optical systems is developed, and two reinforcement regularizers were proposed using this information to improve the quality of the recovered spectral images in a low number of iterations. These regularizers were employed in simulated and real measurements captured in the HDSP laboratory to verify their performance.

Chapter 6 Misalignment correction in compressive spectral imaging designed system via deep learning strategies: This chapter presents an extension that employs a deep learning-based approach to mitigate the effect of the calibration in the CASSI optical system, specifically, this approach deals with this problem by correcting the real measurements using a UNET-based network, and after, the correction employs the ideal sensing matrix to perform the reconstruction process, obtaining a better performance than traditional approach using the real calibrated measurements.

It is important to remark on the contribution to the thesis of each publication, specifically, the papers Garcia et al. (2020a), Hinojosa et al. (2022) and Arguello et al. (2023) allow the study of the optimized codified acquisition in CSI systems and the effect of the implementation in the reconstruction process. In this sense, in Morales-Norato et al. (2023) was presented a detailed characterization of the non-ideal effects, in the sensing process, using a commercial simulation software for remote sensing applications in spectral imaging. On the other hand, in Garcia et al. (2023) the effect of the implementation mismatch in gradient descend-based reconstruction was analyzed, and using this information two regularizers were proposed, also to deal with these bad effects a deep learning approach was developed, first in Jácome et al. (2021) was trained a classification approach and in the conference Contreras et al. (2021) was presented a correction of designed compressive spectral imaging measurements using a deep learning-based Method.

List of Publications

Published journal papers

1. **Hans Garcia**, Claudia V Correa, Henry Arguello, (2020), Optimized sensing matrix for single pixel multi-resolution compressive spectral imaging, **IEEE Transactions on Image Processing**.

2. **Hans Garcia**, Jorge Bacca, Brendt Wohlberg, Henry Arguello, (2023), Calibration Reinforcement Regularizations for Optimized Snapshot Spectral Imaging, **Applied Optics**.

3. Henry Arguello, Jorge Bacca, Hasindu Kariyawasam, Edwin Vargas, Miguel Marquez, Ramith Hettiarachchi, **Hans Garcia**, Kithmini Herath, Udith Haputhanthri, Balpreet Singh Ahluwalia, Peter So, Dushan N Wadduwage, Chamira US Edussooriya, (2023), Deep optical coding design in computational imaging, **Signal processing Magazine**.

4. Román Jácome, Carlos López, **Hans Garcia**, Henry Arguello, (2021), Deep Learning-Based Object Classification for Spectral Images, **Communications in Computer and Information Science**.

5. Carlos Hinojosa, Karen Sanchez, **Hans Garcia**, Henry Arguello, (2022), C-3SPCD: coded aperture similarity constrained design for spatio-spectral classification of single-pixel measurements, **Applied Optics**.

6. David Norato, Sergio Urrea, **Hans Garcia**, Julian Rodriguez, Henry Arguello, Elizabeth

Martinez Ayala, Alberto Silva, Rafael Torres, Ignacio Acero, Francisco Hernández, Lorena Cárdenas, Sonia Rincón, (2023), Hyperspectral Camera as Compact Payload Architecture for Remote Sensing Applications, **Applied Optics**.

On going papers

1. Sergio Urrea, Roman Jacome, MS Asif, Henry Arguello, **Hans Garcia**, DoDo: Double DOE Optical System for Multishot Spectral Imaging, **Submitted**.

2. Romario Gualdron-Hurtado, **Hans Garcia**, Henry Arguello y Jorge Bacca, Unrolled Learned Propagation Model Regularizer for Compressive Spectral Imaging, **On going**.

Conference papers

1. **Hans Garcia**, Julian Rodriguez-Ferreira, Sonia Rincón, Ignacio Acero, Francisco Luis Hernández Torres, Jesus Gonzalez-Llorente, LORENA CARDENAS, MAIRA CAMILA PABA MEDINA, Cristian Esteban Arango, David Ardila, Henry Arguello, (2021), MISC-3 A COLOMBIAN CUBESAT 3U FOR EARTH OBSERVING APPLICATIONS, **72nd International Astronautical Congress**.

2. **Hans Garcia**, Miguel Marquez, Henry Arguello, (2020), Super-Resolution in Compressive Coded Imaging Systems via l2-l1-l2 Minimization Under a Deep Learning Approach, **2020 Data Compression Conference (DCC)**.

3. Ghiordy Contreras, Jhon Pabón, **Hans Garcia**, Fernando Rojas, Henry Arguello, (2021), Correction of Designed Compressive Spectral Imaging Measurements Using a Deep Learning-

Based Method, **XXIII Symposium on Image, Signal Processing and Artificial Vision (STSIVA)**.

4. Juan Cuadrado, Elizabeth Martinez, **Hans Garcia**, Fernando Rojas, Henry Arguello, (2021), Image Reconstruction Performance Analysis by Optical Implementation in Compressive Spectral Imaging, **2021 XXIII Symposium on Image, Signal Processing and Artificial Vision (STSIVA)**.

5. Julian Rodriguez-Ferreira, Kevin Tautiva, Harley GarcÃa, Leandro Rojas, Henry Arguello, and **Hans Garcia** (2023), Implementación de un sensor óptico de concentración de CO2 atmosférico basado en espectroscopÃa láser de diodo sintonizable, **Congreso Colombiano y Conferencia Internacional en Calidad de Aire y Salud Pública - CASAP IX.**

6. Karen Sanchez, Carlos Hinojosa, **Hans Garcia**, Henry Arguello, Sergio Castillo, (2021), Compressed-domain Classification Algorithm for Spectral Imaging Based on Designed Single-Pixel Camera Codification, **Computational Optical Sensing and Imaging**.

7. Crisostomo Barajas-Solano; **Hans Garcia**; Henry Arguello, (2019), Convolutional Basis Pursuit Denoising of Spectral Images Using a Tri-Dimensional Sparse Representation, **2019 XXII Symposium on Image, Signal Processing and Artificial Vision (STSIVA)**.

8. Edson Mojica, **Hans Garcia**, Henry Arguello, (2019), Impact of Multi-resolution reconstruction on Computed Tomography, **2019 XXII Symposium on Image, Signal Processing and Artificial Vision (STSIVA)**.

9. Crisostomo Barajas-Solano, Juan Ramirez, **Hans Garcia**, Henry Arguello, (2019), Tridimensional Convolutional Sparse Coding of Spectral Images, **Hyperspectral Imaging and Sounding of the Environment**.

10. Andrés Jerez, Samuel Pinilla, **Hans Garcia**, Henry Arguello, (2019), Target identification from coded diffraction patterns via template matching, **2019 27th European Signal Processing Conference (EUSIPCO)**.

11. Jhon Angarita, Samuel Pinilla, **Hans Garcia**, Henry Arguello, (2019), Multi-resolution Reconstruction Algorithm for Phase Retrieval in X-ray Crystallography, **2019 27th European Signal Processing Conference (EUSIPCO)**.

12. Elizabeth Martinez, Camilo Calderón, **Hans Garcia**, Henry Arguello, (2020), MRI brain tumour segmentation using a cnn over a multi-parametric feature extraction, **2020 IEEE Colombian Conference on Applications of Computational Intelligence (IEEE ColCACI 2020)**.

13. Carlos López, Román Jácome, **Hans Garcia**, Henry Arguello, (2020), Object classification using spectral images and deep learning, **2020 IEEE Colombian Conference on Applications of Computational Intelligence (IEEE ColCACI 2020)**.

14. Manuel Herrera-Poveda, David Norato, **Hans Garcia**, Sergio Castillo, Andrés Jerez, and Henry Arguello (2023), Multi-domain Discrete Spectral Image Fusion via Implicit Neural Representation, **Computational Optical Sensing and Imaging (COSI)**.

15. Karen Fonseca, **Hans Garcia**, Felipe da Silva, Henry Arguello, and Jorge Bacca (2023), Joint Deep Learning Optical Band Selection and Classification Method for Spectral Data, **Computational Optical Sensing and Imaging (COSI)**.

16. Yesid Romario Hurtado, **Hans Garcia**, Henry Arguello, and Jorge Bacca (Accepted 2023), Learning a Spatially-Variant Propagation Model for Compressive Spectral Imaging, **Computational Optical Sensing and Imaging (COSI)**.

17. Pablo Gomez, **Hans Garcia**, and Henry Arguello (2023), Computational Algorithm for Soil Organic Carbon Percentage Estimation through NIR Spectroscopy, **Computational Optical Sensing and Imaging (COSI)**.

18. Sergio Urrea, Roman Jacome, Salman Asif, Henry Arguello, and **Hans Garcia** (2023), Optical Solutions for Spectral Imaging Inverse Problems with a Shift-Variant System, **LXCV at ICCV 2023**.

Directed/co-directed thesis

1. **Undergrad thesis**, Diseño y construcción de un prototipo funcional de un exoesqueleto de brazo para pacientes con lesión en el plexo braquial, **Oliver Fabian Avila Tamayo, Johan Enrique Gallo Chacon**, 2017.

2. **Undergrad thesis**, Clasificación de objetos empleando imágenes espectrales y aprendizaje de máquina, **Carlos Eduardo López Joya**, 2019.

3. **Undergrad thesis**, Diseño y modelamiento matemático de un sistema optoelectrónico multisensor para adquisición de información espectral y de profundidad, **Juan Pablo Cuadrado Flechas, Elizabeth Juliana Martinez Ayala, Sergio Andres Urrea Vecino**, 2021.
4. **Undergrad thesis**, Implementación de los módulos electrónicos de un sensor de concentración de CO2 atmosférico basado en espectroscopía laser de diodo sintonizable embarcado como carga útil en el globo sonda estratosférico E3Tratos, **Jairo Andrés Camacho Guerrero, Leandro Sebasthyan Rojas Rodríguez**, 2021.
5. **Undergrad thesis**, Implementación de un sensor de concentración de CO2 atmosférico basado en espectroscopía láser de diodo sintonizable embarcado como carga útil en el globo sonda estratosférico e3tratos, **Harley Fernando García Robles, Kevin Andrés Tautiva Salazar**, 2023.
6. **Master thesis**, Desarrollo de una herramienta para la captura y procesamiento de información sobre el estado de los bosques utilizando UAVs, **Arnold Guarin Ramirez**, 2019.
7. **Master thesis**, Near-infrared optoelectronic system for soil organic carbon percentage estimation, **Pablo Andres Gomez Toloza**, On going.
8. **Master thesis**, Optical calibration enhancement algorithm for the implementation of a designed compressive spectral imaging system, **Sergio Andrés Urrea Vecino**, On going.
9. **Master thesis**, Design of an end-to-end model for band selection in material classification using spectral signatures captured in the near-infrared spectrum, **Karen Andrea Fonseca**

Estupiñan, On going.

2. Theoretical background

2.1. Spectral Imaging (SI)

Spectral imagery is composed of two spatial dimensions (x,y), and one dimension in the wavelength domain λ. Thus, the spectral bands are the intensities at each λ in which the object is measured. Depending on the range of analyzed wavelengths, spectral images can be classified as ultraviolet (UV) (200-380nm), visible (380-780nm) or infrared (IF) (780nm-50000nm). These images differ to the traditional gray scale images in that each spatial point contains a complete spectrum instead of just an intensity value Roman-Gonzalez and Vargas-Cuentas (2014). Furthermore, the amount of measured bands is used to classify SI as: multi-spectral images that contain tens of bands, or hyper-spectral images that refer to those with up to hundreds of bands. The information contained in SI makes them applicable to several areas such as ground-cover classification, mineral exploration, and agricultural assessment in remote sensing GA Shaw (2003); biomedical imaging Lu and Fei (2014) for which SI offer great potential for noninvasive disease diagnosis and surgical guidance; identification of military objectives in surveillance and security applications Stellman et al. (2001) among others.

There are several methods for acquiring a spectral image, and a common characteristic of many of these methods is that they require scanning the area of interest as illustrated in Fig. 1. For instance, an approach that captures the spectrum for a single point is called Whisk-broom spectrometer Green et al. (1998); another approach acquires all the spatial pixels for each wavelength at a time, which is known as filtered camera Duarte et al. (2008); on the other hand, the pushbroom spectrometer measures the spectra across a spatial line and then scans the scene across the other spatial dimension Mouroulis and McKerns (2000). All of the aforementioned methods require acquiring a massive amount of data, given that they rely on the Nyquist-Shannon theorem Jerri (1977); Landau (1967). In addition, the scanning-based methods have low sensing speed and high complexity processing and storage.

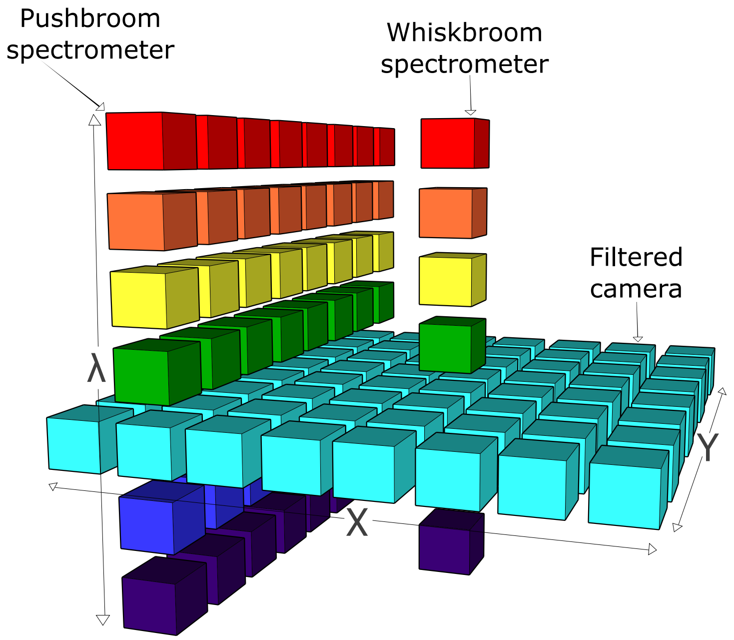

Figura 1. Scanning spectral imaging approaches for a spectral data cube with X and Y as spatial coordinates and λ the wavelengths Garcia et al. (2016).

2.2. Codified compressive spectral imaging systems

An alternative sampling theory is called compressed sensing (CS) Donoho (2006); Takhar et al. (2006); Baraniuk and Steeghs (2007), which proposes to perform compression and sampling in a single process. Specifically, CS establishes that it is possible to retrieve a signal from a small number of samples under some given conditions. Thus, instead of acquiring MNL samples (voxels), CS captures $k \ll NML$ random projections of the scene. The sensing process can be represented in matrix form as $\mathbf{y}_0 = \mathbf{H}_0\mathbf{x} + \mathbf{w}$, where $\mathbf{w}$ represents the system noise and the sensing matrix $\mathbf{H}_0$ models the linear interaction between the scene and the optical elements such as coding elements, prisms, gratings, and other elements that contain the optical system. It is important to remark, given that the number of measurements is considerably smaller than the number of voxels, the inverse problem given by $\hat{\mathbf{x}} = \mathbf{H}_0^{-1}\mathbf{y}$, is ill conditioned, leading to an infinite number of solutions. Therefore, reconstruction of the signal $\mathbf{x}$ is obtained using compressed sensing optimization algorithms that take advantage of the sparse representation of $\mathbf{x}$ in some transformation basis $\boldsymbol{\Psi}$. Specifically, these algorithms obtain an approximation of $\boldsymbol{\theta}$ with the optimization problem given by

$$\hat{\mathbf{x}} = \boldsymbol{\Psi}\{argmin_{\theta}\left(||\mathbf{H}_0\boldsymbol{\Psi}\boldsymbol{\theta} - \mathbf{y}||_2^2 + \tau||\boldsymbol{\theta}||_1^2\right)\} \tag{1}$$

where τ is a regularization parameter. It is important to remark that other regularizers that try to improve the quality of the reconstructions in simulation and testbed systems can be used, some of these without previous knowledge as total variation (TV) Bian et al. (2018); or l2 prior deep learning-based Garcia et al. (2020b); Song et al. (2020).

In recent years, different optical architectures have been developed to implement the compressive sampling theory for the acquisition of spectral images, which has been termed compressive spectral imaging (CSI). Figure 2 shows some of the most representative compressive spectral imaging architectures that are based on transmissive elements, like digital micromirror device (DMD) or printed coded apertures. The Spatial-Spectral Encoded Compressive HS Imager (SSCSI) is built by combining optical spatial and spectral modulation which provides a high degree of randomness in the measured projections and the sparsity-constrained reconstruction algorithm Lin et al. (2014a); the coded aperture snapshot spectral imager (CASSI) uses a coded aperture and one or more dispersive elements to modulate the optical field from a scene while a detector captures a 2-dimensional, multiplexed projection of the three-dimensional data cube representing the scene Wagadarikar et al. (2008a); the dual-coded hyper-spectral imager (DCSI) separately codes both spatial and spectral dimensions within a single exposure, achieving an independent spectral code for each sensor pixel, DCSI facilitates flexible capture modes customized for different applications

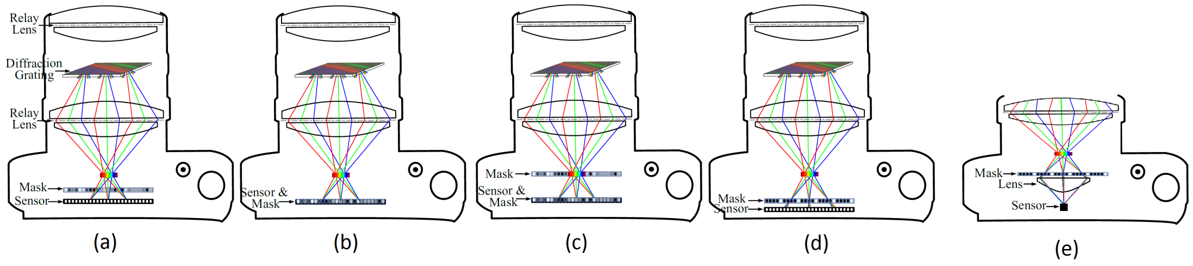

Figura 2. Most representative CSI optical architectures (a) Coded Mask (SSCSI) Lin et al. (2014a), (b) Coded Aperture CASSI Wagadarikar et al. (2008a), (c)Dual Coded Mask DCSI Lin et al. (2014b), (d) Prism and Mask PMVIS Cao et al. (2011) and (e) SPC Duarte et al. (2008). Source:Lin et al. (2014a)

Lin et al. (2014b); the prism-mask multispectral video imaging system (PMVIS) is composed of an occlusion mask, a prism, and a grayscale camera, the radiance from the scene is sampled by the occlusion mask to avoid overlap among spectra on the image plane, spatial and angular smoothness in reflectance is assumed for each captured scene point, so that the light rays sampled by a mask hole have the same radiance Cao et al. (2011); the single pixel camera (SPC) which is an optical device comprising a DMD, two lenses, a single photon detector, and an analog-to-digital (A/D) converter, computes random linear measurements of the scene under view in a single measure Duarte et al. (2008).

On the other hand, another popular kind of optical codification element is called diffractive optical elements (DOE) Arguello et al. (2021), which are widely used in recent years, given that the DOE is phase coding-based allowing high light transmittance in CSI systems. Usually, the DOE-based optical systems can be modeled by a convolution between the response of the system, called the point spread function, and the input scene, which also can be written as matrix multiplication in a similar way that DMD-based systems. It is important to remark that DOEs codifications also can be designed for the reconstruction task on spectral imaging improving the performance Arguello et al. (2023). Each of these architectures presents its own advantages and drawbacks for different applications. However, all of them require some specific design in the codification elements to allow accomplishing some mathematical requirements, for example, the RIP to allows obtaining high-quality reconstructions

Arguello and Arce (2012), which cannot be guaranteed exactly on testbed implementation.

3. Optimized codified system design analysis

an In this section a review of a state-of-the-art strategy to design the codification of linearly modeled optical systems based on compressive sensing to acquire spectral images is described. Specifically, the optimization problem presented in (1) can be solved using iterative gradient-based methods, where the matrix $\mathbf{H}_0$ has a particular structure given by the optical elements and their configuration within the system Cao et al. (2016) (See Fig. 3(left) for an illustrative example of the CASSI system $\mathbf{H}_0$ matrix). Despite this fixed structure, usually, snapshot imaging systems have free-optical parameters, that can be adjusted to improve the reconstruction quality, i.e., there are distributions of these free-values that produce better quality than others Arce et al. (2014) for the specific task that is designed. For instance, one optimization criterion that is used, for the reconstruction task, is the restricted isometry property (RIP) Arce et al. (2014), in particular, this approach establishes that given an image $\mathbf{x}_0$ and some sensing matrix $\mathbf{H}_0$, it is possible to obtain the following relation

$$\lambda_{\min}(\mathbf{H}_0\mathbf{H}_0^T)||\mathbf{x}_0||_2^2 \leq ||\mathbf{H}_0\mathbf{x}_0||_2^2 \leq \lambda_{\max}(\mathbf{H}_0\mathbf{H}_0^T)||\mathbf{x}_0||_2^2, \tag{2}$$

where $\lambda_{\min}(\cdot)$ and $\lambda_{\max}(\cdot)$ represent the minimum and maximum eigenvalues of a matrix. Some state-of-the-art designs are based on concentrating the non-zero eigenvalues of $\mathbf{H}_0$ as much as possible, maintaining the structure of the matrix Mejia and Arguello (2018); Hinojosa et al. (2018); Arguello and Arce (2014a); Cuadros et al. (2014); Elad (2007); Hong and Zhu (2018). For instance,

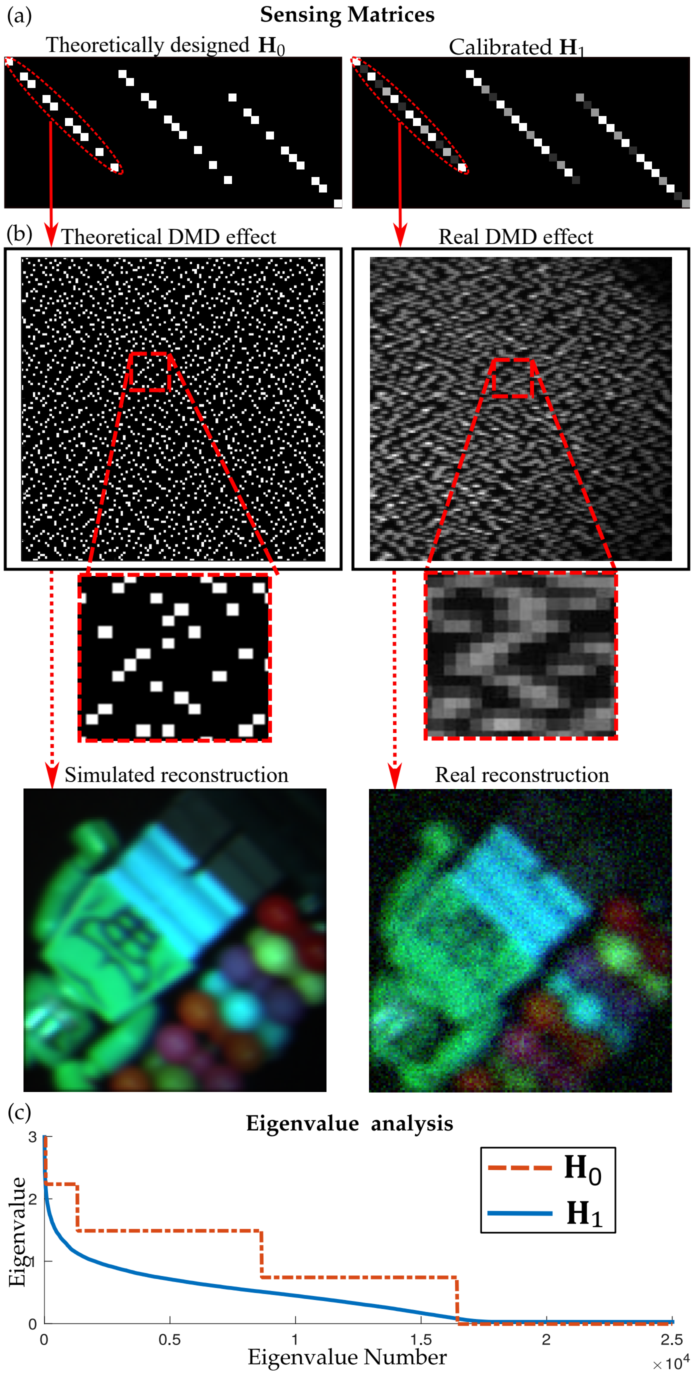

Figura 3. (left) (a) the designed sensing matrix $\mathbf{H}_0$ and (b) the designed, coded aperture (free-parameters), (right) (a) the calibrated matrix $\mathbf{H}_1$ obtained into the CASSI system implemented, together with the (b) calibrated coded aperture, and (c) an eigenvalue analysis, where it can evident that the eigenvalue distribution of the calibrated matrix $\mathbf{H}_1$ is worst than the theoretically designed $\mathbf{H}_0$.

if $\mathbf{H}_0$ has an SVD decomposition of the form

$$\mathbf{H}_0 = \mathbf{U}\left[\sqrt{c}\mathbf{I}\ \ \mathbf{0}\right]\mathbf{V}, \tag{3}$$

for $\mathbf{U}$ and $\mathbf{V}$ as arbitrary orthonormal matrices, (3) indicates that the non-zero eigenvalues of $\mathbf{H}_0^T\mathbf{H}_0$ are all equal to c. Therefore, the work in Arguello and Arce (2014a); Cuadros et al. (2014); Elad (2007); Hong and Zhu (2018) showed that an optimal sensing strategy can be found by solving the following optimization problem

$$\mathbf{H}_0 = \arg\min_{\mathbf{H}} ||\mathbf{H}^T\mathbf{H} - c\mathbf{I}||_F^2, \tag{4}$$

for a constant $c > 0$, which leads to the kind of matrix here referred to as designed. It is important to remark that the $\mathbf{H}_0$, and $\mathbf{H} \in \mathbb{R}^{m\times n}$ matrices are not square matrices because $m < n$ as in a snapshot spectral imaging system. To analyze the quality of the designed sensing matrix $\mathbf{H}_0$ in terms of convergence speed, the lemma 3.0.1 is developed, which allows concluding that a good sensing matrix design conducts faster convergence in a gradient-based reconstruction algorithm.

Lemma 3.0.1. *Given the optimization problem*

$$\mathbf{x}^* = \arg\min_{\mathbf{x}_0} f_0(\mathbf{x}_0) := \frac{1}{2}||\mathbf{y}_0 - \mathbf{H}_0\mathbf{x}_0||_2^2 + \tau_1\varphi(\mathbf{x}_0), \tag{5}$$

a constant $0 < \mu < 1$*, an initialization* $\mathbf{x}_0^{(0)}$*, and a bounded smooth regularization* $||\nabla\varphi(\mathbf{x}_0^{(k)})||_2^2 \leq L$

Chan et al. (2016), the iterations of a gradient-descent are given by

$$\begin{aligned}\mathbf{x}_0^{(k+1)} &= \mathbf{x}_0^{(k)} - \mu \nabla f_0(\mathbf{x}_0^{(k)}) \\ &= \mathbf{x}_0^{(k)} - \mu(\mathbf{H}_0^T(\mathbf{y}_0 - \mathbf{H}_0\mathbf{x}_0^{(k)}) + \tau_1 \nabla \varphi(\mathbf{x}_0^{(k)})),\end{aligned} \tag{6}$$

which converges to

$$||\mathbf{x}_0^{(k+1)} - \mathbf{x}^*||_2^2 \leq q_0^k ||\mathbf{x}_0^{(0)} - \mathbf{x}^*||_2^2 + \frac{\mu \tau_1 L}{1 - q_0}, \tag{7}$$

where $\mathbf{x}^*$ *is the reference image and* $q_0 < 1$ *as* $q_0 = \text{máx}\left\{|1 - \mu\lambda_{\min}(\mathbf{H}_0\mathbf{H}_0^T)|, |1 - \mu\lambda_{\max}(\mathbf{H}_0\mathbf{H}_0^T)|\right\}$.

Demostración. From $f_0(\mathbf{x}_0) = \frac{1}{2}||\mathbf{y}_0 - \mathbf{H}_0\mathbf{x}_0||_2^2 + \tau_1 \varphi(\mathbf{x}_0)$ we have that

$$\begin{aligned}&||\mathbf{x}_0^{(k+1)} - \mathbf{x}^*||_2^2 = \\ &||\mathbf{x}_0^{(k)} - \mu(\mathbf{H}_0^T(\mathbf{H}_0\mathbf{x}_0^{(k)} - \mathbf{y}_0) + \tau_1 \nabla \varphi(\mathbf{x}_0^{(k)})) - \mathbf{x}^*||_2^2\end{aligned} \tag{8}$$

since, $\mathbf{y}_0 = \mathbf{H}_0\mathbf{x}^*$ we have that

$$\begin{aligned}&||\mathbf{x}_0^{(k+1)} - \mathbf{x}^*||_2^2 = \\ &= ||\mathbf{x}_0^{(k)} - \mathbf{x}^* - \mu\mathbf{H}_0^T\mathbf{H}_0(\mathbf{x}_0^{(k)} - \mathbf{x}^*) - \mu\tau_1 \nabla \varphi(\mathbf{x}_0^{(k)}))||_2^2 \\ &= ||(\mathbf{I} - \mu\mathbf{H}_0^T\mathbf{H}_0)(\mathbf{x}_0^{(k)} - \mathbf{x}^*) - \mu\tau_1 \nabla \varphi(\mathbf{x}_0^{(k)}))||_2^2 \\ &\leq ||\mathbf{I} - \mu\mathbf{H}_0^T\mathbf{H}_0||_2^2 ||\mathbf{x}_0^{(k)} - \mathbf{x}^*||_2^2 + \mu\tau_1 ||\nabla \varphi(\mathbf{x}_0^{(k)}))||_2^2 \\ &\leq q_0 ||\mathbf{x}_0^{(k)} - \mathbf{x}^*||_2^2 + \mu\tau_1 L\end{aligned} \tag{9}$$

where the last step in (9) comes from the triangular and Cauchy inequalit, $\mathbf{y}_0 = \mathbf{H}_0\mathbf{x}^*$, and that

$q_0 = \text{máx}\left\{|1-\mu\lambda_{\min}(\mathbf{H}_0\mathbf{H}_0^T)|, |1-\mu\lambda_{\max}(\mathbf{H}_0\mathbf{H}_0^T)|\right\}$. Applying the recursion and since $q_0 < 1$ we have that

$$\begin{aligned} ||\mathbf{x}_0^{(k+1)} - \mathbf{x}^*||_2^2 &\leq q_0 \left(\dots (q_0 ||\mathbf{x}_0^{(0)} - \mathbf{x}^*||) + \mu\tau_1 L \right) + \mu\tau_1 L \\ &\leq q_0^k ||\mathbf{x}_0^{(0)} - \mathbf{x}^*|| + \mu\tau_1 L \sum_{j=0}^{k-1} q_0^{j+1} \\ &\leq q_0^k ||\mathbf{x}_0^{(0)} - \mathbf{x}^*||_2^2 + \mu\tau_1 L \sum_{j=0}^{k-1} q_0^{j} \\ &\leq q_0^k ||\mathbf{x}_0^{(0)} - \mathbf{x}^*||_2^2 + \frac{\mu\tau_1 L}{1-q_0}, \end{aligned} \tag{10}$$

where the last term comes from the closed-form of geometric series Li (1959). □

From the results shown in lemma 3.0.1 is possible to conclude that the solution of the optimization problem in (4), which aims to concentrate the eigenvalues of $\mathbf{H}_0$, induces a faster convergence than a random matrix.

4. Impact of calibration

This chapter developed an analysis of the impact of non-ideal characteristics in a CSI designed optical system implementation in a reconstruction task, only taking into account the loss of performance by the calibration of the designed sensing matrix. Remarking that random values, following a Gaussian Candès and Wakin (2008) or Bernoulli distribution Zhang et al. (2010), are usually employed to set the free parameters of the codification in CSI systems, due to their ease of generation, making random encoders popular and widely used Marwah et al. (2013). However, random entries are not the optimal solution for these entries; they can be designed for specific systems and applications, attaining gains of up to one order of magnitude in different quality metrics Bacca et al. (2021); Arguello et al. (2023). Among the most popular applications are compressive spectral imaging Correa et al. (2016), single-pixel camera Garcia et al. (2020a), Fourier Ptychography Jagatap et al. (2019), microscopy Kellman et al. (2019), and Compressive Tomography Ma et al. (2020). In particular, the free-parameters of $\mathbf{H}_0$ are designed by adopting hand-crafted assumptions Correa et al. (2015); Mejia and Arguello (2018); Garcia et al. (2020a), theoretical constraints such as the mutual coherence or the concentration of measure Arguello and Arce (2014a); Cuadros et al. (2014); Elad (2007); Hong and Zhu (2018), or recent deep learning strategies such as end-to-end (E2E) Bacca et al. (2020); Wang et al. (2018); Bacca et al. (2019b); Arguello et al. (2023). The idea behind most of these designs is to improve the invertibility properties of $\mathbf{H}_0$, such as the concentration of its eigenvalues that allows its easy inversion by gradient-based reconstruction methods Arce et al. (2014); Rueda et al. (2015); Galvis et al. (2017); Arguello and Arce

(2014b), which allows traditional iterative reconstruction approaches to obtain a high performance, converging in a low number of iterations in simulated scenarios. For instance, in Mejia and Arguello (2018), authors presented a theoretical sensing matrix design that enhances the reconstructions from simulated data by up to 12dB of PSNR compared with a random matrix in simulations. Also, the work in Hinojosa et al. (2018) obtains a classification accuracy boost of 8 % against random patterns.

Once the sensing matrix $\mathbf{H}_0$ has been theoretically designed and verified in simulations, the free parameters of coding elements are carefully manufactured or configured according to the design, and implemented in an optical setup to acquire the scenes. Usually, a mismatch occurs between the physical implementation and the theoretically designed sensing matrix $\mathbf{H}_0$ because of implementation issues such as fabrication errors in lenses, prism, coding and the other optical elements. For instance, in Rueda-Chacon et al. (2019) the designed pixelated optical filters are not perfectly square as expected, exhibiting sloped edges due to the lift-off fabrication process; in Baek et al. (2020) the point spread function achieved by the fabricated diffractive optical elements (DOE) forms a larger convolutional kernel than expected, due to the low-diffraction efficiency of the real DOE. These examples and others, as the chromatic aberrations of the lens, and the mismatch between the pitch of the sensor and the encoding elements Choi et al. (2021), force researchers to conduct a detailed characterization of the system known as calibration. The exhaustive calibration process is carried out to obtain the calibrated sensing matrix $\mathbf{H}_1$ Arguello et al. (2013). It is important to remark that the calibrated sensing matrix $\mathbf{H}_1$ is not exactly equal to the designed $\mathbf{H}_0$, but, $\mathbf{H}_1$ is the sensing matrix that exactly models the real implemented system, where the mismatch of the models can be expressed as $\mathbf{H}_1 = \mathbf{H}_0 + \mathbf{H}_2$ with the mismatch matrix $\mathbf{H}_2$ calculated in the calibration step. However, most of the recovery algorithms in spectral imaging do not provide good performance when the calibrated sensing matrix $\mathbf{H}_1$ is employed, as it does not have the same invertibility properties as the theoretically designed matrix $\mathbf{H}_0$. An illustrative example of this effect can be seen in Fig.3. There, the matrix structures of the theoretically designed and calibrated sensing matrices for the coded aperture snapshot spectral imager (CASSI) Wagadarikar et al. (2008b) are shown in Fig. 3 (a). Also in Fig. 3 (b) the free parameters from the DMD effect include an illustration of the reconstructed image in each case, and in Fig. 3 (c) a conditionality analysis of the sensing matrices is illustrated, where it is shown that the calibrated matrix $\mathbf{H}_1$ has a worst conditionally than the theoretically designed $\mathbf{H}_0$, in terms of the distribution of the eigenvalues.

It is important to remark that the matrix $\mathbf{H}_2$ cannot be exactly estimated before implementation of the system. To show this, in Fig. 4 some convolutional kernels were used in the designed coding to try to simulate the mismatch present in the implementation, where the complexity of obtaining an acceptable mismatch model before the implementation is evident. Commonly, the simplest solution to these problems is to avoid the design step and relegate it for future work Tian et al. (2014); Yeh et al. (2017). Contrarily, some works have acknowledged the calibration implementation problem, and proposed numerical solutions, for example, the work in Sitzmann et al. (2018) adds small random perturbations to the DOE heights in the design process to make a robust decoder to mismatches in the implemented height map compared with the design one; also, in Baek et al. (2020) in the real implementation step needs to take some measurements and update

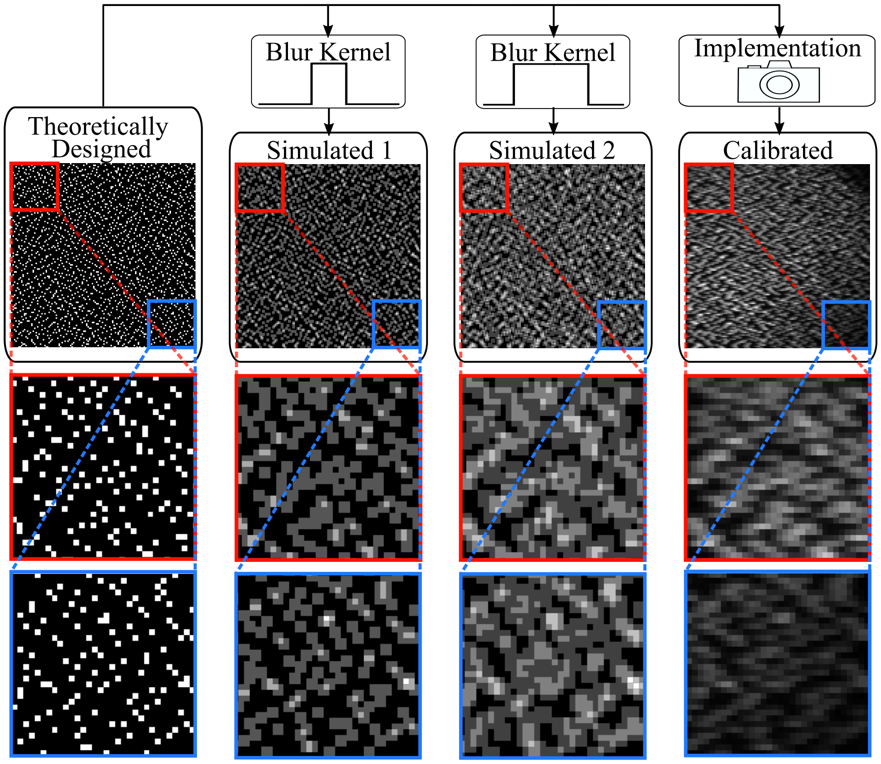

Figura 4. Comparison of the real calibration DMD encoding obtained from the calibration process with the theoretically designed and two attempts to emulate the mismatch using using two blur convolution kernel with different windows size.

the decoder (retraining the deep decoder model) to fit this new system, or in Arguello et al. (2013) developing a high-order model completely different from the simulated one to improve precision and less dependent on calibration.

To obtain the spectral image, regularized gradient-based iterative methods are typically used, with the calibrated sensing matrix $\mathbf{H}_1$ as the real forward operator, in this way, some of the recent efforts have been based on designing new and robust priors or methodologies to recover the signal. For instance, plug-and-play (PnP) methods Venkatakrishnan et al. (2013); Chan et al. (2016) elevate the concept of regularizers by using an off-the-shelf image denoising algorithm with a non-apparent closed-form expression as prior. Recently, calibrated regularization by denoising

(C-RED) Xie et al. (2020) considered the calibration process into the algorithm, i.e., the optical procedure to obtain the calibrated sensing matrix $\mathbf{H}_1$ is incorporated in the recovery algorithm to ensure the accuracy of the sensing model. Nonetheless, it is important to remark that C-RED does not solve the mismatch problem of quality loss in the reconstruction of real measurements since it finds $\mathbf{H}_1$, which is the real sensing matrix but does not allow to take advantage of the designed mathematical characteristics of $\mathbf{H}_0$. Other mathematical approaches as preconditions are used to improve the condition of the problem Calvetti (2007). However, finding a suitable preconditions matrix is complex, especially, when the sensing matrix is non-square Saad (2003) as the case of snapshots spectral imaging.

4.1. Calibrated sensing matrix analysis

After achieving the best possible recovery quality in simulations by optimizing the free optical parameters of $\mathbf{H}_0$, the optimal parameters are placed and aligned in a real setup. Later, calibration takes place to determine the non-ideal characteristics of the implemented system, this process, for example, consist of illuminating a perfectly reflective material with uniform light to characterize each of the available parameters of the sensing matrix, and captures the real implemented values as follows

$$(\mathbf{H}_1)_{i,j} = \mathcal{R}\{(\mathbf{H}_0)_{i,j}\} + \omega_{i,j} \quad for\, i,j \subseteq \Omega, \tag{11}$$

where $\mathcal{R}\{\cdot\}$ represents the effect of the real implementation process, $\omega_{i,j}$ is the additive Gaussian noise present in the process which can be different for each pixel (i,j), and Ω represents the set of indices of the free-parameters in the sensing matrix. For instance, in the CASSI system, calibration can be performed by illuminating the perfectly reflective material with a band-to-band illumination Rueda et al. (2015), and for the DOE-based system, the point spread function (PSF) is acquired through a point source with band-to-band illumination Arguello et al. (2021). This process ensures that $\mathbf{H}_1$ is the exact sensing matrix of the implemented optical setup.

However, due to the calibration process, $\mathbf{H}_1$ does not preserve the same invertibility properties of the designed matrix $\mathbf{H}_0$, as it was illustrated in Fig.3. Without loss of generality, we assume that $\mathbf{H}_0$ and $\mathbf{H}_1$ are normalized, i.e., $||\mathbf{H}_0\mathbf{H}_0^T||_2^2 = 1$ and $||\mathbf{H}_1\mathbf{H}_1^T||_2^2 = 1$, which ensure $\lambda_{\max}(\mathbf{H}_0\mathbf{H}_0^T) = \lambda_{\max}(\mathbf{H}_1\mathbf{H}_1^T) = 1$. This thesis focused on reducing the implementation effect on the systems where the calibration problem produces $\lambda_{\min}(\mathbf{H}_1\mathbf{H}_1^T) < \lambda_{\min}(\mathbf{H}_0\mathbf{H}_0^T)$; consequently, the implemented setup does not take advantage of the invertibility properties of the designed one. Therefore, using the result of Lemma 3.0.1 it is possible to conclude that the convergence of the real system $\mathbf{H}_1$ is slower compared with the designed one $\mathbf{H}_0$.

5. Calibration Reinforcement Regularizations for Optimized Snapshot Spectral Imaging

In this chapter, two proposed reinforcement regularizers that aim to reduce the unwanted effect in the reconstruction because of the implementation process shown in Fig. 3 are presented. To model these non-ideal characteristics in the implementation presented in section 4, which affect the desired reconstruction performance, the calibrated sensing matrix $\mathbf{H}_1$ can be represented as the sum of the designed matrix and an additional matrix, i.e., $\mathbf{H}_1 = \mathbf{H}_0 + \mathbf{H}_2$, where $\mathbf{H}_2$ represents the mismatch between the calibrated/implemented and the designed/simulated sensing models. Note that the mismatch matrix can be calculated as $\mathbf{H}_2 = \mathbf{H}_1 - \mathbf{H}_0$ since $\mathbf{H}_1$ and $\mathbf{H}_0$ are known. Therefore, the real snapshot measurements $\mathbf{y}_1$ can be expressed as

$$\mathbf{y}_1 = \underbrace{(\mathbf{H}_0 + \mathbf{H}_2)}_{\mathbf{H}_1}\mathbf{x}^* + \mathbf{w} = \mathbf{y}_0 + \mathbf{y}_2 + \mathbf{w}, \tag{12}$$

where $\mathbf{x}^*$ represents the acquired spectral image, $\mathbf{H}_2$ stands for the calculated mismatch matrix, $\mathbf{y}_0 = \mathbf{H}_0\mathbf{x}^*$ are the designed/simulated measurements, $\mathbf{y}_2$ are the mismatch measurements given by $\mathbf{y}_2 = \mathbf{H}_2\mathbf{x}^*$ and $\mathbf{w}$ is the noise of the system. Given, the measurements $\mathbf{y}_1$, the spectral image $\mathbf{x}^*$ can be estimated using different recovery algorithms Chan et al. (2016); Bacca et al. (2019a,b), for simplicity, in this project, a gradient descent algorithm is used to illustrate the effect of the calibration system in the recovery process. However, a more sophisticated algorithm can be used as will be illustrated in the simulations Section 5.4.

The traditional ℓ_2 optimization problem, referred as $f_1(\mathbf{x}_1)$ can be expressed as

$$\min_{\mathbf{x_1}} f_1(\mathbf{x}_1) = \frac{1}{2}||(\mathbf{H}_0 + \mathbf{H}_2)\mathbf{x}_1 - \mathbf{y}_1||_2^2 + \tau_1 \varphi(\mathbf{x}_1). \tag{13}$$

Where it is important to remark that in an ideal case $\mathbf{x}_1 \approx \mathbf{x}^*$, therefore the solution through gradient descent iterations, indexed by k, is given by

$$\mathbf{x}_1^{(k+1)} = \mathbf{x}_1^{(k)} - \mu(\mathbf{H}_1^T(\mathbf{H}_1\mathbf{x}_1^{(k)} - \mathbf{y}_1) + \tau_1 \nabla\varphi(\mathbf{x}_1^{(k)})). \tag{14}$$

Let $\mathbf{x}_1^{(k)}$ be the iteration with real measurements in (14), and $\mathbf{x}_0^{(k)}$ as the designed iteration in (6). It is worth noting that if iterations in (6) and (14) start from the same point, i.e., $\mathbf{x}_1^{(0)} = \mathbf{x}_0^{(0)}$, the estimation difference at the first iteration is given by

$$\begin{aligned} \mathbf{x}_0^{(1)} - \mathbf{x}_1^{(1)} &= \mathbf{x}_0^{(0)} - \mu\nabla f_0(\mathbf{x}_0^{(0)}) - \mathbf{x}_1^{(0)} + \mu\nabla f_1(\mathbf{x}_1^{(0)}) \\ &= \mu\left(\nabla f_1(\mathbf{x}_1^{(0)}) - \nabla f_0(\mathbf{x}_0^{(0)})\right). \end{aligned} \tag{15}$$

Then, following the iteration process, it is possible to obtain

$$\mathbf{x}_0^{(k+1)} - \mathbf{x}_1^{(k+1)} = \mu \sum_{i=0}^{k} \left(\nabla f_1(\mathbf{x}_1^{(i)}) - \nabla f_0(\mathbf{x}_0^{(i)})\right), \tag{16}$$

where the cumulative gradient difference is given by the differences of the points in each iteration. Specifically, the term $\nabla f_1(\mathbf{x}_1^{(i)}) - \nabla f_0(\mathbf{x}_0^{(i)})$ is given by

$$
\begin{aligned}
\nabla f_1(\mathbf{x}_1^{(i)})-\nabla f_0(\mathbf{x}_0^{(i)}) &= \mathbf{H}_1^T(\mathbf{H}_1\mathbf{x}_1^{(i)}-\mathbf{y}_1)-\mathbf{H}_0^T(\mathbf{H}_0\mathbf{x}_0^{(i)}-\mathbf{y}_0) \\
&\quad + \tau_1(\nabla\varphi(\mathbf{x}_0^{(i)}) - \nabla\varphi(\mathbf{x}_1^{(i)})) \\
&= \mathbf{H}_0^T(\mathbf{H}_1\mathbf{x}_1^{(i)}-\mathbf{y}_1)+\mathbf{H}_2^T(\mathbf{H}_1\mathbf{x}_1^{(i)}-\mathbf{y}_1)-\mathbf{H}_0^T(\mathbf{H}_0\mathbf{x}_0^{(i)}-\mathbf{y}_0)+\varepsilon_i \\
&= \mathbf{H}_0^T\mathbf{H}_0(\mathbf{x}_1^{(i)}-\mathbf{x}_0^{(i)})+\mathbf{H}_0^T(\mathbf{H}_2\mathbf{x}_1^{(i)}-\mathbf{y}_2)+\mathbf{H}_2^T(\mathbf{H}_1\mathbf{x}_1^{(i)}-\mathbf{y}_1)+\varepsilon_i, \qquad (17)
\end{aligned}
$$

where the second line comes from $\mathbf{H}_1 = \mathbf{H}_0 + \mathbf{H}_2$, and $\varepsilon_i = \tau_1(\nabla\varphi(\mathbf{x}_0^{(i)}) - \nabla\varphi(\mathbf{x}_1^{(i)}))$ stands for the difference between the regularization terms. Therefore, the difference between the two iteration points in the k-th iteration for the calibration problem is given by the following lemma.

Lemma 5.0.1. *Considering $\mathbf{x}_1^{(k)}$ as the iteration of the optimization problem with real measurements as in* (14)*, $\mathbf{x}_0^{(k)}$ denoting the designed iteration given by* (6)*, and modelling the calibrated sensing matrix $\mathbf{H}_1 = \mathbf{H}_0 + \mathbf{H}_2$; the difference between the solutions of the designed problem $f_0(\mathbf{x}_0)$ and the optimization problem with real measurements $f_1(\mathbf{x}_1)$ at the iteration $k+1$, i.e., $\mathbf{x}_0^{(k+1)} - \mathbf{x}_1^{(k+1)}$ if $\mathbf{x}_1^{(0)} = \mathbf{x}_0^{(0)}$ is given by*

$$
\begin{aligned}
\mathbf{x}_0^{(k+1)} - \mathbf{x}_1^{(k+1)} = \mu \sum_{i=0}^{k} (\mathbf{I} - \mathbf{H}_0^T\mathbf{H}_0)^{(k-i)} \Big(& \mathbf{H}_0^T(\mathbf{H}_2\mathbf{x}_1^{(i)} - \mathbf{y}_2) \\
& + \mathbf{H}_2^T(\mathbf{H}_1\mathbf{x}_1^{(i)} - \mathbf{y}_1) \Big) + \varepsilon_k, \qquad (18)
\end{aligned}
$$

where ε_k is the propagated error by the differences in the regularization on each iteration.

Demostración. Denoting as $\mathbf{x}_1^{(k)}$ the designed iteration in (14) and $\mathbf{x}_0^{(k)}$ as the (6), if they start for the same value i.e. $\mathbf{x}_1^{(0)} = \mathbf{x}_0^{(0)}$, we have that

$$\begin{aligned}
&\mathbf{x}_0^{(1)} - \mathbf{x}_1^{(1)} = \mathbf{x}_0^{(0)} - \mu\nabla f_0(\mathbf{x}_0^{(0)}) - \mathbf{x}_1^{(0)} + \mu\nabla f_1(\mathbf{x}_1^{(0)}) + \mu\varepsilon_0\\
&= \mu\left(\nabla f_1(\mathbf{x}_1^{(0)}) - \nabla f_0(\mathbf{x}_1^{(0)}) + \varepsilon_0\right)\\
&= \mu\Big(\mathbf{H}_0^T(\mathbf{H}_0\mathbf{x}_1^{(0)} + \mathbf{H}_2\mathbf{x}_1^{(0)} - \mathbf{y}_0 - \mathbf{y}_2) + \mathbf{H}_2^T(\mathbf{y}_1 - \mathbf{H}_1\mathbf{x}_1^{(0)})\\
&- \mathbf{H}_0^T(\mathbf{H}_0\mathbf{x}_1^{(0)} - \mathbf{y}_0) + \varepsilon_0\Big)\\
&= \mu\left(\mathbf{H}_0^T(\mathbf{H}_2\mathbf{x}_1^{(0)} - \mathbf{y}_2) + \mathbf{H}_2^T(\mathbf{H}_1\mathbf{x}_1^{(0)} - \mathbf{y}_1) + \varepsilon_0\right)\\
&= \mu\left(\mathrm{R}\big(\mathbf{x}_1^{(0)}\big) + \varepsilon_0\right),
\end{aligned} \tag{19}$$

where $\varepsilon_0 = \tau_1(\nabla\varphi(\mathbf{x}_1^{(0)}) - \nabla\varphi(\mathbf{x}_1^{(0)}))$ and

$$\mathrm{R}\big(\mathbf{x}_1^{(i)}\big) = \left(\mathbf{H}_0^T(\mathbf{H}_2\mathbf{x}_1^{(i)} - \mathbf{y}_2) + \mathbf{H}_2^T(\mathbf{H}_1\mathbf{x}_1^{(i)} - \mathbf{y}_1)\right),$$

following the iteration process, we have that

$$\mathbf{x}_0^{(2)} - \mathbf{x}_1^{(2)} = \mathbf{x}_0^{(1)} - \mu\nabla f_0(\mathbf{x}_0^{(1)}) - \mathbf{x}_1^{(1)} + \mu\nabla f_1(\mathbf{x}_1^{(1)}). \tag{20}$$

Replacing (19) into (20) we have that

$$\begin{aligned}
\mathbf{x}_0^{(2)} - \mathbf{x}_1^{(2)} &= \mu\left(\mathrm{R}\big(\mathbf{x}_1^{(0)}\big) + \varepsilon_0 + \nabla f_1(\mathbf{x}_1^{(1)}) - \nabla f_0(\mathbf{x}_0^{(1)})\right) \\
&= \mu\Big(\mathrm{R}\big(\mathbf{x}_1^{(0)}\big) + \mathbf{H}_0^T\mathbf{H}_0\mathbf{x}_1^{(1)} - \mathbf{H}_0^T\mathbf{H}_0\mathbf{x}_0^{(1)} + \\
&\mathbf{H}_0^T(\mathbf{H}_2\mathbf{x}_1^{(1)} - \mathbf{y}_2) + \mathbf{H}_2^T(\mathbf{H}_1\mathbf{x}_1^{(1)} - \mathbf{y}_1) + \varepsilon_1\Big) \\
&= \mu\Big(\mathrm{R}\big(\mathbf{x}_1^{(0)}\big) + \mathbf{H}_0^T\mathbf{H}_0(\mathbf{x}_1^{(1)} - \mathbf{x}_0^{(1)}) + \\
&\mathbf{H}_0^T(\mathbf{H}_2\mathbf{x}_1^{(1)} - \mathbf{y}_2) + \mathbf{H}_2^T(\mathbf{H}_1\mathbf{x}_1^{(1)} - \mathbf{y}_1) + \varepsilon_1\Big) \\
&= \mu\Big((\mathbf{I} - \mathbf{H}_0^T\mathbf{H}_0)\mathrm{R}\big(\mathbf{x}_1^{(0)}\big) + \\
&\mathbf{H}_0^T(\mathbf{H}_2\mathbf{x}_1^{(1)} - \mathbf{y}_2) + \mathbf{H}_2^T(\mathbf{H}_1\mathbf{x}_1^{(1)} - \mathbf{y}_1) + \varepsilon_1\Big) \\
&= \mu\left((\mathbf{I} - \mathbf{H}_0^T\mathbf{H}_0)\mathrm{R}\big(\mathbf{x}_1^{(0)}\big) + \mathrm{R}\big(\mathbf{x}_1^{(1)}\big) + \varepsilon_1\right), \qquad (21)
\end{aligned}$$

where $\varepsilon_1 = \varepsilon_0 + \tau_1(\nabla\varphi(\mathbf{x}_1^{(1)}) - \nabla\varphi(\mathbf{x}_0^{(1)}))$ is the accumulated gradient regularization error. Following the iteration process for step 3, the expression is given by

$$\begin{aligned}
\mathbf{x}_0^{(3)} - \mathbf{x}_1^{(3)} = \mu\Big(&(\mathbf{I} - \mathbf{H}_0^T\mathbf{H}_0)^2\mathrm{R}\big(\mathbf{x}_1^{(0)}\big) \\
&+ (\mathbf{I} - \mathbf{H}_0^T\mathbf{H}_0)\mathrm{R}\big(\mathbf{x}_1^{(1)}\big) + \mathrm{R}\big(\mathbf{x}_1^{(2)}\big), + \varepsilon_2\Big),
\end{aligned} \qquad (22)$$

using a recursive method and mathematical simplifications, in a similar way that was obtained (22), the difference between the designed $\mathbf{x}_0$ and experimental $\mathbf{x}_1$ points was generalized for the $k+1$

iteration, which can be expressed as

$$\begin{aligned}\mathbf{x}_0^{(k+1)} - \mathbf{x}_1^{(k+1)} = \mu \sum_{i=0}^{k} (\mathbf{I} - \mathbf{H}_0^T \mathbf{H}_0)^{(k-i)} \Big(& \mathbf{H}_0^T (\mathbf{H}_2 \mathbf{x}_1^{(i)} - \mathbf{y}_2) \\ & + \mathbf{H}_2^T (\mathbf{H}_1 \mathbf{x}_1^{(i)} - \mathbf{y}_1) \Big) + \varepsilon_k, \end{aligned} \tag{23}$$

where ε_k is the propagated error by the difference between regularization on each iteration. □

The strategy of this thesis is to reduce the difference in (18). The reduction of $||\mathbf{x}_0^{k+1} - \mathbf{x}_1^{k+1}||_2^2$ let the iterations of the implemented system $\mathbf{x}_1^{k+1}$ go near to the iteration of the theoretical designed system $\mathbf{x}_0^{k+1}$. It is important to remark that the matrix $\mathbf{H}_0$, $\mathbf{H}_1$ and $\mathbf{H}_2$ are fixed and known from the implemented optical setup, while $\mathbf{y}_2$ are unknown. Consequently, the difference through the iteration directly depend on the terms $\mathbf{H}_0^T (\mathbf{H}_2 \mathbf{x}_1^{(i)} - \mathbf{y}_2) + \mathbf{H}_2^T (\mathbf{H}_1 \mathbf{x}_1^{(i)} - \mathbf{y}_1)$.

5.1. Reinforcement ℓ_2 gradient Regularization

The differences in each iteration presented in Lemma 5.0.1 are analyzed in (18). In order to guide the solution of the experimental system $\mathbf{x}_1^k$ to the direction of the designed $\mathbf{x}_0^k$, it is required to reduce the error between the designed problem and the optimization problem with real measurements, which is mainly given by the terms $\mathbf{H}_0^T(\mathbf{H}_2\mathbf{x}_1^{(i)} - \mathbf{y}_2) + \mathbf{H}_2^T(\mathbf{H}_1\mathbf{x}_1^{(i)} - \mathbf{y}_1)$. From (18), and using the triangular Cauchy inequality with a boundary regularizer $||\nabla\varphi(x)||_2^2 \leq L$, the magnitue of $\mathbf{x}_0^{(k+1)} - \mathbf{x}_1^{(k+1)}$ can be estimated as

$$\begin{aligned}&||\mathbf{x}_1^{(k+1)} - \mathbf{x}_0^{(k+1)}||_2^2 \leq \\ &\mu\sum_{i=0}^{k}||(\mathbf{I} - \mathbf{H}_0^T\mathbf{H}_0)^{(k-i)}||_2^2\Big(||\mathbf{H}_0^T(\mathbf{H}_2\mathbf{x}_1^{(i)} - \mathbf{y}_2)||_2^2 \\ &+ ||\mathbf{H}_2^T(\mathbf{H}_1\mathbf{x}_1^{(i)} - \mathbf{y}_1)||_2^2)\Big) + 2\mu L. \qquad (24)\end{aligned}$$

Equation (24) establishes a bound for the distance between the experimental and designed iteration using the gradient descent method. Notice that in (24) there are two terms that depend on the iterative estimation $\mathbf{x}_1^{(i)}$. These two terms are the central core of the proposed method in this chapter since they are used as regularizers in the proposed approaches described in the subsections 5.2 and 5.3.

5.2. Reinforcement regularizer without estimating $\mathbf{y}_2$

An approach is proposed to reduce the error term in each iteration, which takes into account the term that depends only on $\mathbf{x}_1^{(i)}$ and the known $\mathbf{y}_1$ in (24). Specifically, by including an additional reinforced regularization term in the optimization problem as

$$\begin{aligned}\underset{\mathbf{x_a}}{\text{mín}} f_a(\mathbf{x}_a) := \frac{1}{2}||\mathbf{H}_1\mathbf{x}_a - \mathbf{y}_1||_2^2 + \tau_1\varphi(\mathbf{x}_a) + \\ \frac{\tau_3}{2}||\mathbf{H}_2^T(\mathbf{H}_1\mathbf{x}_a - \mathbf{y}_1)||_2^2.\end{aligned} \tag{25}$$

The last term $||\mathbf{H}_2^T(\mathbf{H}_1\mathbf{x}_a - \mathbf{y}_1)||_2^2$ in (25) is the proposed regularization that conduces to mitigating one of the two additional terms of (24). The inclusion of the proposed regularization allows a faster convergence for some values of τ_3 following the result in Theorem 5.2.1, which set a condition on τ_3 to show that the proposed regularizer obtains a faster convergence compared with baseline ℓ_2 approach based on $f_1(\mathbf{x}_1)$ (13) for the gradient-descent method. These conditions depend on the matrices $\mathbf{H}_0$ and $\mathbf{H}_2$, and the parameters τ_3 and μ.

Theorem 5.2.1. *Defining* $p_a = ||\mathbf{I} - \mu\left(\mathbf{H}_1^T\mathbf{H}_1 + \tau_3\mathbf{H}_1^T\mathbf{H}_2\mathbf{H}_2^T\mathbf{H}_1\right)||_2^2$, $q_0 = ||\mathbf{I} - \mu\mathbf{H}_0^T\mathbf{H}_0||_2^2$, $q_1 = ||\mathbf{I} - \mu\mathbf{H}_1^T\mathbf{H}_1||_2^2$ *and employing k-th iteration of a gradient-descent with loss functions* $f_0(\mathbf{x}_0)$, $f_1(\mathbf{x}_1)$ *and* $f_a(\mathbf{x}_a)$, *we have that*

$$||\mathbf{x}_0^{k+1} - \mathbf{x}^*||_2^2 \leq ||\mathbf{x}_a^{k+1} - \mathbf{x}^*||_2^2 \leq ||\mathbf{x}_1^{k+1} - \mathbf{x}^*||_2^2.$$

where $\mathbf{x}^*$ *is the solution;* $\mathbf{x}_0^{(k+1)}$, $\mathbf{x}_1^{(k+1)}$ *and* $\mathbf{x}_a^{(k+1)}$ *stands for the gradient-descent iteration of the main loss functions for the designed* $f_0(\mathbf{x}_0)$, *traditional* $f_1(\mathbf{x}_1)$*; and proposed* $f_a(\mathbf{x}_a)$ *case, respectively, if* $q_0 \leq p_a \leq q_1$.

Demostración. Similar as the proof of Lemma 3.0.1, the convergence rate of $f_1(\mathbf{x}_1) = \frac{1}{2}||\mathbf{y}_1 -$

$\mathbf{H}_1\mathbf{x}_1||_2^2 + \tau_1\varphi(\mathbf{x}_1)$ is given as

$$||\mathbf{x}_1^{(k+1)} - \mathbf{x}^*||_2^2 \leq q_1^k||\mathbf{x}_1^{(0)} - \mathbf{x}^*||_2^2 + \frac{\mu\tau_1 L}{1-q_1}. \tag{26}$$

where $q_1 = ||\mathbf{I} - \mu\mathbf{H}_1^T\mathbf{H}_1||_2^2$. On the other hand, from the proposed main function $f_a(x)$ we have that

$$||\mathbf{x}_a^{(k+1)} - \mathbf{x}^*||_2^2 = ||\mathbf{x}_a^{(k)} - \mu(\nabla f_a(\mathbf{x}_a^{(k)}) + \tau_1\nabla\varphi(\mathbf{x}_a^{(k)})) - \mathbf{x}^*||_2^2, \tag{27}$$

where $\nabla f_a(\mathbf{x})$ is given by

$$\begin{aligned}\nabla f_a(\mathbf{x}_a) &= \nabla f_1(\mathbf{x}_a) + \tau_3\mathbf{H}_1^T\mathbf{H}_2\mathbf{H}_2^T\mathbf{H}_1(\mathbf{x}_a - \mathbf{x}^*)\\ &= (\mathbf{H}_1^T\mathbf{H}_1 + \tau_3\mathbf{H}_1^T\mathbf{H}_2\mathbf{H}_2^T\mathbf{H}_1)(\mathbf{x}_a - \mathbf{x}^*),\end{aligned} \tag{28}$$

therefore, we have that

$$\begin{aligned}||\mathbf{x}_a^{(k+1)}-\mathbf{x}^*||_2^2 &= ||\mathbf{x}_a^{(k)}-\mathbf{x}^*-\mu(\mathbf{B}_1(\mathbf{x}_a^{(k)}-\mathbf{x}^*)+\tau_1\nabla\varphi(\mathbf{x}_a^{(k)}))||_2^2\\ &= ||(\mathbf{I} - \mu\mathbf{B}_1)(\mathbf{x}_q^{(k)} - \mathbf{x}^*) - \mu\tau_1\nabla\varphi(\mathbf{x}_a^{(k)})||_2^2\\ &\leq ||\mathbf{I} - \mu\mathbf{B}_1||_2^2||\mathbf{x}_a^{(k)} - \mathbf{x}^*||_2^2 + \mu\tau_1 L,\end{aligned} \tag{29}$$

where the last step in (29) comes from the triangular and Cauchy inequality and $\mathbf{B}_1 = \mathbf{H}_1^T\mathbf{H}_1 +$

$\tau_3 \mathbf{H}_1^T \mathbf{H}_2 \mathbf{H}_2^T \mathbf{H}_1$. Therefore, defining $p_a = ||\mathbf{I} - \mu \mathbf{B_1}||_2^2$ and unrolling the iteration we have

$$\begin{aligned} ||\mathbf{x}_a^{(k+1)} - \mathbf{x}^*||_2^2 &\leq p_a \Big(\dots (p_a ||\mathbf{x}_a^{(0)} - \mathbf{x}^*||) + \mu \tau_1 L \Big) + \mu \tau_1 L \\ &\leq p_a^k ||\mathbf{x}_a^{(0)} - \mathbf{x}^*|| + \mu \tau_1 L \sum_{j=0}^{k-1} p_a^{j+1} \\ &\leq p_a^k ||\mathbf{x}_a^{(0)} - \mathbf{x}^*||_2^2 + \mu \tau_1 L \sum_{j=0}^{k-1} p_a^j \\ &\leq p_a^k ||\mathbf{x}_a^{(0)} - \mathbf{x}^*||_2^2 + \frac{\mu \tau_1 L}{1 - p_a}. \end{aligned} \tag{30}$$

Since $\mathbf{x}_0^{(0)} = \mathbf{x}_a^{(0)} = \mathbf{x}_1^{(0)}$ start for the same iteration and if $q_0 \leq p_a \leq q_1$ we have that

$$||\mathbf{x}_0^{k+1} - \mathbf{x}^*||_2^2 \leq ||\mathbf{x}_a^{k+1} - \mathbf{x}^*||_2^2 \leq ||\mathbf{x}_1^{k+1} - \mathbf{x}^*||_2^2. \tag{31}$$

□

5.3. Reinforcement regularizer estimating $\mathbf{y}_2$

To include also the term that depends on $\mathbf{y}_2$ in (24), two options are explored, the first one is to ignore it as the proposed approach in (25) and the second one consists in including it in a new optimization problem $f_b(\mathbf{x}_b, \mathbf{y}_2)$, which will estimate iteratively the spectral image $\mathbf{x}_b$ and the new variable $\mathbf{y}_2$. Therefore, it is proposed an approach adding two new regularization terms, compared with well-known ℓ_2 in (13), to control the deviation of the solution in each iteration as

$$\begin{aligned}\min_{\mathbf{x_b},\mathbf{y}_2} f_b(\mathbf{x}_b,\mathbf{y}_2) &= \frac{1}{2}||\mathbf{H}_1\mathbf{x}_b-\mathbf{y}_1||_2^2+\tau_1\varphi(\mathbf{x}_b)\\ &+\frac{\tau_2}{2}||\mathbf{H}_0^T(\mathbf{H}_2\mathbf{x}_b-\mathbf{y}_2)||_2^2+\frac{\tau_3}{2}||\mathbf{H}_2^T(\mathbf{H}_1\mathbf{x}_b-\mathbf{y}_1)||_2^2,\end{aligned} \tag{32}$$

where $\mathbf{y}_2$ needs to be estimated as an auxiliary variable, and the last two terms aim at minimizing the mismatch of the model and are exactly the same two extra terms found in (24) which move away the gradient direction in the real case $\mathbf{y}_1$ and $\mathbf{H}_1$ from the designed in (5) which use the simulated/desired measurements $\mathbf{y}_0$ and designed sensing matrix $\mathbf{H}_0$.

5.4. Simulation Results of Calibration Reinforcement Regularization

This section presents simulated experiments to quantify the performance and validate the effectiveness of the two reinforcement regularizers explicitly used in the optimization problems in (25) and (32). Two optical systems, CASSI, and a DOE-based architecture were evaluated employing a designed CA, and a designed DOE, respectively. The theoretically designed $\mathbf{H}_0$ for the CASSI system is based on the criteria explained in (4) Correa et al. (2015) setting to recover a spectral image of size $128 \times 128 \times 13$ with a compression ratio of 0.3365, equivalent to 4 encoded measurements; on the other hand, the DOE-based system was designed according to Jeon et al. (2019) for a spectral image of $64 \times 64 \times 6$ with a compression ratio of 0.5 using a single measurement with an RGB sensor. It is important to remark that for the DOE-based system the structure of the matrix models the convolution operation of the input image with the PSF of the system and for the CASSI system as is illustrated the Fig. 3. These designed sensing matrices were implemented in the laboratory, to obtain their corresponding calibrated sensing matrices $\mathbf{H}_1$ as explained in section 4.1. The step size on gradient descent algorithm μ parameter is chosen as the best value for the baseline ℓ_2 scheme, i.e., without any of the proposed reinforcement regularizers. The τ_2 and τ_3 regularization terms were chosen as the minimum value satisfying the Theorem 5.2.1 as explained in the following section.

Afterward, two main experiments were carried out: first, it was evaluated the level of the mismatch given by the values of the matrix $\mathbf{H}_2$ in (12) and the noise in designed simulated measurements to compare with the baseline problem in (13), referred to as f_1, and $\mathbf{x}_1$ as the estimated image. The loss functions including the first and second reinforcement regularizers indicated in (25) and (32) are denoted as f_a, and f_b, respectively. Furthermore, to easy identify, the recovery images using f_a and f_b are denoted as $\mathbf{x}_a$ and $\mathbf{x}_b$, respectively. Since regularization over $\mathbf{y}_2$ in the optical systems is a hand-craft task, I use a warm start with $\mathbf{y}_2 = \mathbf{H}_2\mathbf{x}_a$, where $\tilde{\mathbf{x}}_a$ is the estimation of the scene employing (25).

5.4.1. Theoretical guarantees. This subsection analyzes the relationship between the existence of a τ_3 parameter, that satisfies Theorem 5.2.1 in (25), with the values of the matrix $\mathbf{H}_2$ of the implemented optical systems. To be as realistic as possible, the spatial distribution of the mismatch matrix $\mathbf{H}_2$ is preserved, i.e., $\mathbf{H}_2 = \mathbf{H}_1 - \mathbf{H}_0$, and the synthetic calibrated sensing matrix $\tilde{\mathbf{H}}_1$ was constructed as

$$\tilde{\mathbf{H}}_1 = \mathbf{H}_0 + \gamma\mathbf{H}_2, \tag{33}$$

where the real calibrated sensing matrix obtained in the laboratory occurs when $\gamma = 1$. Figure 5 illustrates the difference of $p_a - q_1$ varying τ_3 for different level of mismatch γ for a fixed $\mu = 0.001$. It is important to remark that $p_a - q_1$ should be negative to satisfy Theorem 5.2.1, which means that the proposed approach in (25) allows a faster convergence than traditional approach (13). In Fig. 5 can be observed that when the value of γ is higher, i.e., the mismatch matrix $\mathbf{H}_2$ is predominant in the sensing matrix, Theorem 5.2.1 is not easily satisfied for both evaluated systems. Therefore, the inequality $p_a < q_1$ can be treated as a bound of the mismatch criterion between the designed and the real system.

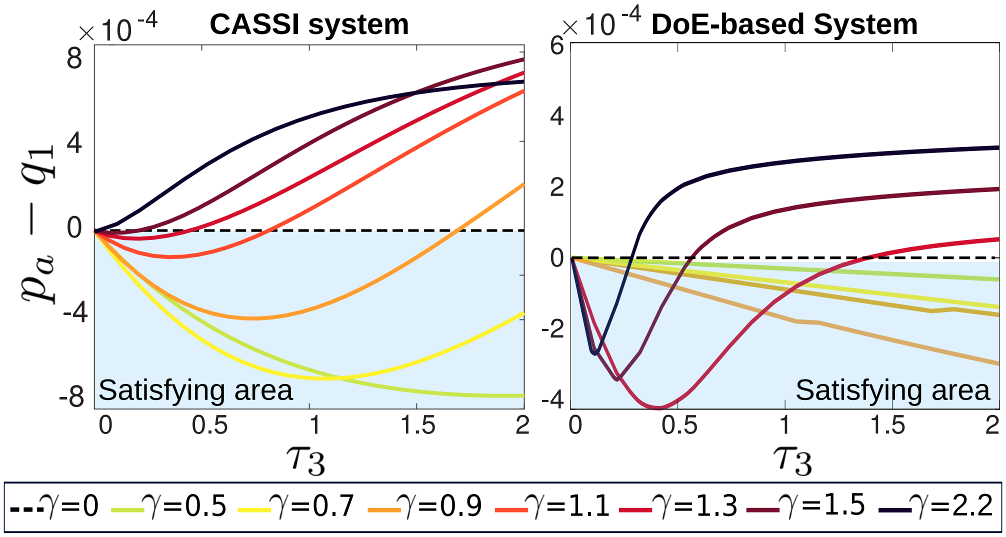

Figura 5. Analysis of τ_3 values that satisfy Theorem 5.2.1 for different γ values for a fixed $\mu = 0.001$. The values that satisfy the theorem are obtained when $p_a - q_1 < 0$. (Left) results for the CASSI system, (Right) for the DOE-based system.

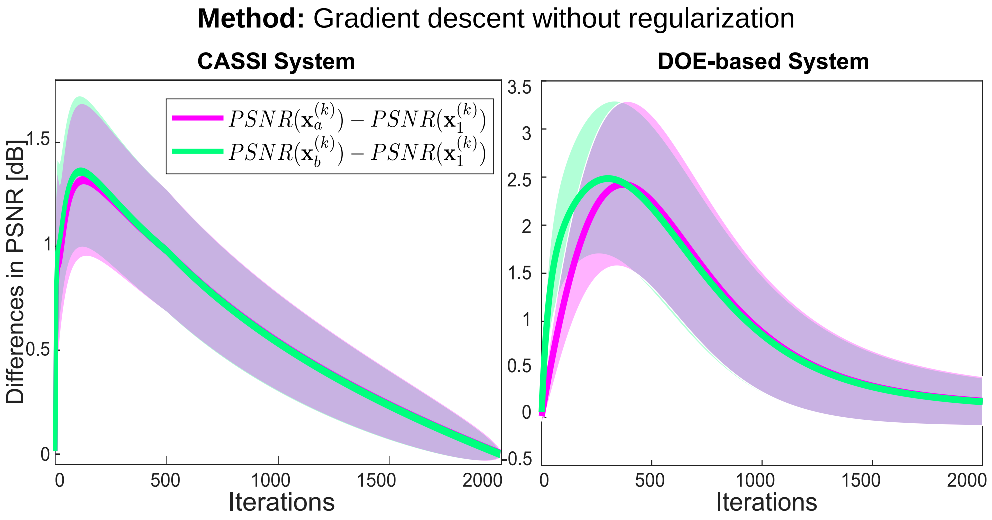

Figura 6. Performance comparison for the gradient iterations of the proposed methods ($\mathbf{x}_a$ and $\mathbf{x}_b$) and the baseline ($\mathbf{x}_1$). The results are the average of 15 spectral images of the CAVE dataset. The positive difference shows that the proposed methods are faster than the experimental baseline.

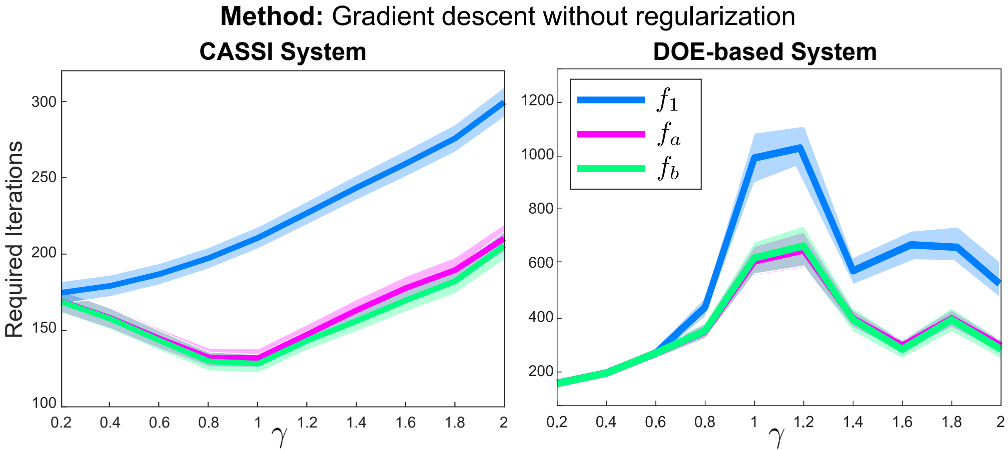

Figura 7. Required number of iterations to obtain a PSNR of 1dB less than the maximum possible performance obtained with baseline (f_1) and the proposed methods (f_a and f_b) for different γ values to analyze the convergence speed.

5.4.2. Performance analysis of the reconstruction approaches using gradient descent. Section 5.4.1 shows that Theorem 5.2.1 is satisfied for the evaluated snapshot spectral imaging systems. To complement these results, this experiment aims to validate the statement that the proposed method converges faster than the baseline $f_1(\cdot)$ cost function, i.e., without the reinforcement terms, calculating the performance difference in each iteration. To this end, $\gamma = 1$ was set as the level of the mismatch matrix. It is worth to emphasize that each iteration of the three main loss functions f_1, f_a and f_b are denoted as $\mathbf{x}_1^{(k)}$, $\mathbf{x}_a^{(k)}$ and $\mathbf{x}_b^{(k)}$, respectively. Figure. 6 illustrates the performance at each iteration of the proposed approaches and that of the baseline for 15 spectral images from the CAVE dataset, using the CASSI and the DOE-based system. It is possible to see the difference in PSNR in the first iterations, which shows that the proposed approaches are faster, as expected by theorem 5.2.1, with an improvement of up to $3dB$. The average maximum value of convergence in PNSR for the 15 images obtained for the baseline f_1 using only gradient descent is 21.17 ± 3.07 dB and 29.97 ± 3.68 for the CASSI and DOE-based systems, respectively. Since all the methods achieved the same performance after many iterations as is shown in 6, in this results is plot the required number of iterations to obtain a fixed quality for both optical architectures. To this end, it is set the desired performance for each image as 1dB less than the maximum obtained by the baseline approach, and an analysis of the effect on the convergence using the proposed method under different mismatch levels measured by γ is carried on. These results are depicted in Fig. 7, where the baseline f_1 approach requires more iterations than the proposed approaches to obtain the same performance; furthermore, when γ takes high values, the gap decreases compared with the results from $\gamma = 1$, and the behavior is similar for both architectures.

5.5. Extensions of the reinforcement regularizers for the PnP approach

Since the proposed method includes regularizers to the traditional recovery methods, this section shows how to add the reinforced regularizer into a more recent recovery algorithm referred to as Plug-and-Play FISTA Kamilov et al. (2017a). For this particular case, two different approaches are proposed, depending on the prior knowledge or the initialization of $\mathbf{y}_2$, in a similar way to the one presented in section 5.1.

5.5.1. Reinforced Plug-and-Play without estimating $\mathbf{y}_2$.

In applications where prior information or initialization of the vector $\mathbf{y}_2$ is not available, the complexity of the inverse problem increases since it is necessary to estimate alternatively an additional variable $\mathbf{y}_2$, to avoid this computational cost, it is proposed to minimize (25) using PnP-FISTA, where the proximal operator given by the regularizer $\varphi(\mathbf{x}_a)$ is replaced with a general denoiser $\mathcal{D}_{\sigma_k}(\cdot)$ of strength $\sigma_k = \sqrt{\mu\tau_1}$ Kamilov et al. (2017b). The complete steps of the PnP-FISTA are shown in Algorithm 1. This PnP scheme maintains the gradient-descent formulation, validated in Theorem 5.2.1, but using a denoiser that does not have an implicit smooth optimization formulation, such as the block-matching and 3D filtering (BM3D) Dabov et al. (2007) or recursive filter (RF) Gastal and Oliveira (2011).

Algorithm 1 C-PnP-FISTA: Without estimating $\mathbf{y}_2$

```
initialization
repeat
    $\mathbf{z}^{(k)} = \mathbf{s}^{(k-1)} - \mu \nabla f_a(\mathbf{s}^{(k-1)})$
    $\bar{\mathbf{x}}_a^{(k)} = \mathcal{D}_{\sigma_k}\left(\mathbf{z}^{(k)}\right)$
    $q_{(k)} = \frac{1}{2}\left(1 + \sqrt{1 + 4q_{(k-1)}^2}\right)$
    $\mathbf{s}^{(k)} = \bar{\mathbf{x}}_a^{(k)} + ((q_{(k-1)} - 1)/q_{(k)})(\bar{\mathbf{x}}_a^{(k)} - \bar{\mathbf{x}}_a^{(k-1)})$
until the stopping criterion is satisfied
```

5.5.2. Reinforced Plug-and-Play estimating $\mathbf{y}_2$:. In optical imaging setups, having an initialization of $\mathbf{y}_2$ is indeed possible. For these cases, it is proposed to minimize (32), estimating $\bar{\mathbf{x}}_b$ and $\mathbf{y}_2$, using alternating minimization, and a denoiser such as the BM3D of the form

$$\bar{\mathbf{x}}_b^{(k)} = \arg\min_{\bar{\mathbf{x}}_b} f_b\left(\bar{\mathbf{x}}_b, \mathbf{y}_2^{(k-1)}\right), \tag{34}$$

$$\mathbf{y}_2^{(k)} = \arg\min_{\bar{\mathbf{x}}_b} f_b\left(\bar{\mathbf{x}}_b^{(k)}, \mathbf{y}_2\right). \tag{35}$$

Each subproblem is solved using a gradient-based method. In particular, for (34), this work used the PnP-FISTA and for (35) a gradient descent as is described in Algorithm 2. Note that in line 4, the gradient is calculated with respect to $\bar{\mathbf{x}}_b$ and $\mathbf{y}_2$ is treated as a constant. Similarly, in line 9, the gradient-descent step is calculated with respect to $\mathbf{y}_2$.

Algorithm 2 C-PnP-FISTA: Estimating $\mathbf{y}_2$

```
initialization
repeat
    for $i = 1$ to $T_1$ do
        $\mathbf{z}^{(i)} = \mathbf{s}^{(i-1)} - \mu \nabla_{\mathbf{x}_b} f_b(\mathbf{s}^{(i-1)}, \mathbf{y}_2^{(i-1)})$
        $\bar{\mathbf{x}}_b^{(i)} = \mathcal{D}_{\sigma_i}\left(\mathbf{z}^{(i)}\right)$
        $q_{(i)} = \frac{1}{2}\left(1 + \sqrt{1 + 4q_{(i-1)}^2}\right)$
        $\mathbf{s}^{(i)} = \bar{\mathbf{x}}_b^{(i)} + ((q_{(i-1)} - 1)/q_{(i)})(\bar{\mathbf{x}}_b^{(i)} - \bar{\mathbf{x}}_b^{(i-1)})$
    end for
    for $i = 1$ to $T_2$ do
        $\mathbf{y}_2^{(i)} = \mathbf{y}_2^{(i-1)} - \mu \nabla_{\mathbf{y}_2} f_b(\mathbf{s}^{(i-1)}, \mathbf{y}_2^{(i-1)})$
    end for
until the stopping criterion is satisfied
```

5.5.3. Performance analysis of the reconstruction approaches using PnP-FISTA.

Similar to the gradient descent approach results, simulations for the PnP-FISTA-based approaches were performed to analyze the convergence speed and performance of the proposed methods. Figure 8 shows the PSNR of each iteration of the proposed methods compared with the baseline $f_1 + \varphi$ approach, i.e., without the reinforcement regularization terms and using a PnP-FISTA algorithm. It can be seen that the proposed approaches converge faster than the baseline, and the proposed pair of reinforcement regularizers denoted as $f_b + \varphi$ are the fastest overall. Furthermore, it can be observed that all methods converge in 200 PnP-FISTA iterations, where the performance of the proposed method is up to 5dB better than the baseline. Also, Fig. 9 indicates the required number of iterations required by each method to achieve 21.5dB, at different mismatch levels γ. It is worth noting that the baseline approach requires more iterations to obtain the same performance than the proposed approaches; this plot also verifies the intuition that in the case of high γ values, the

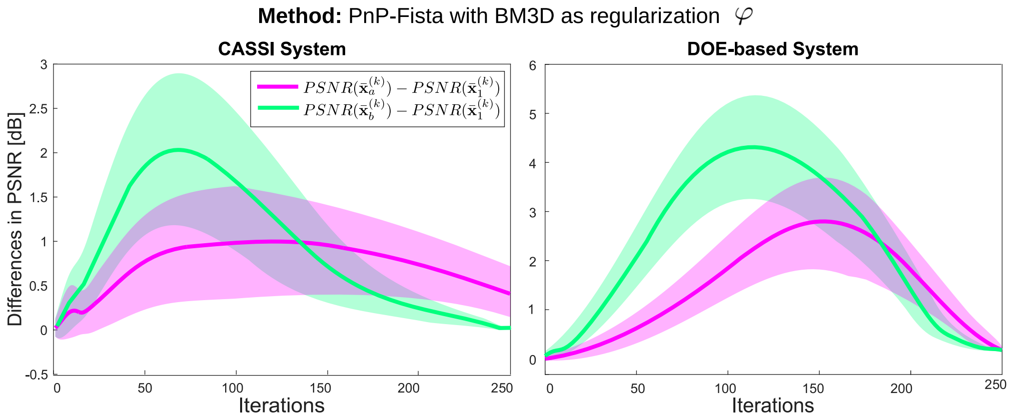

Figura 8. Performance difference through the gradient iterations between the solution of the proposed methods ($\bar{\mathbf{x}}_a$ and $\bar{\mathbf{x}}_b$), and the baseline ($\bar{\mathbf{x}}_1$) using BM3D regularization in all cases, where $PSNR(\mathbf{x}^{(k)})$ refer to the PSNR between the spectral image $\mathbf{x}^*$ and the reconstructed one using each approach.

improvement of the proposed approach is reduced.

On the other hand, taking into account that the PnP approaches include a denoiser as a regularizer, an analysis of the noise effect was conducted for the CASSI optical system. Figure 10 shows the ratio of the required iteration to obtain the same final performance for the proposed methods (f_a and f_b) concerning the traditional approach at different SNR levels. It is possible to observe that the proposed methods need less iteration to obtain the same performance, even in the low SNR scenario.

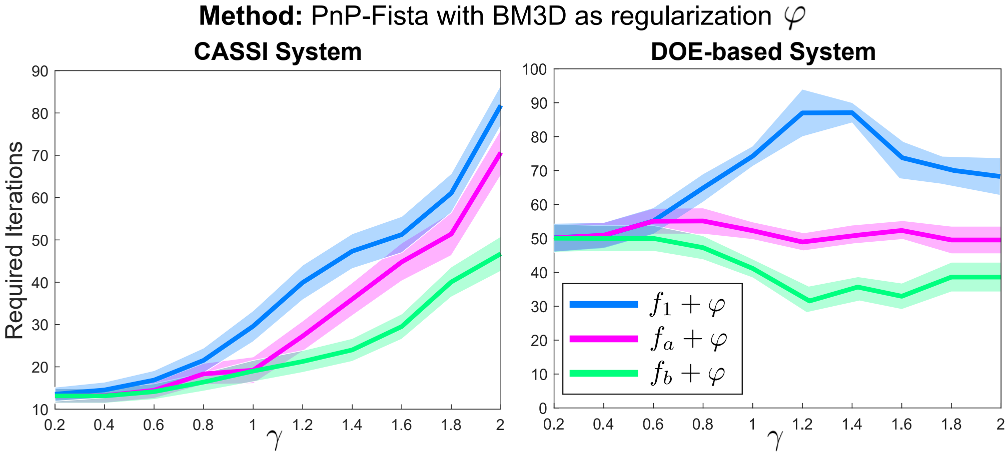

Figura 9. Required number of iterations to obtain a PSNR of 1dB less than the maximum obtained with the baseline ($f_1+\varphi$) and the proposed methods ($f_a+\varphi$ and $f_b+\varphi$) for different γ values to analyze the convergence speed.

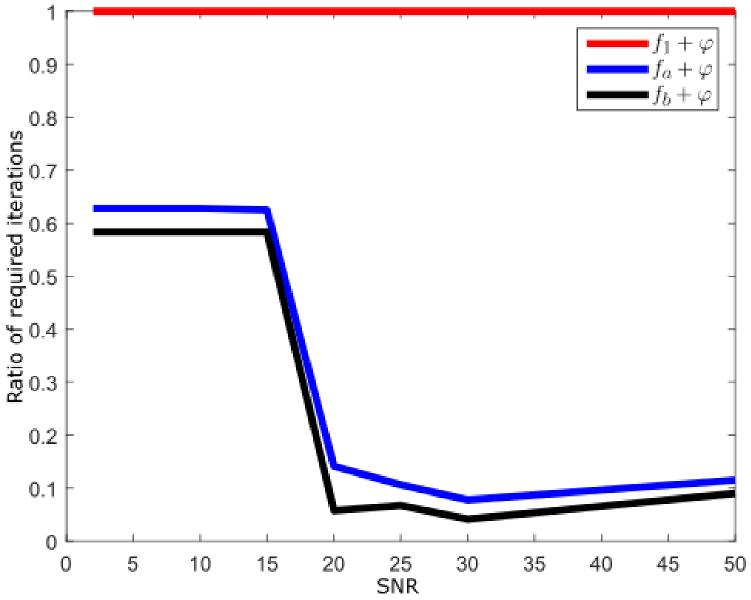

Figura 10. Ratio of required iterations to obtain the same PSNR performance at different SNR levels, where 1 means the required iterations for the traditional approach.

5.5.4. Experimental validation. An optical test-bed of CASSI was implemented, to experimentally verify the proposed reconstruction methodology. Specifically, the CASSI system shown in Fig. 11 was built using an 8*mm* navitar objective lens, a 100*mm* doublet relay lens; a digital micromirror device (DMD) digital light innovations DLI4130VIS-7XGA as encoding element; a 100*mm* doublet as a relay; a custom made Amici prism as a dispersive element; and a STINGRAY F-080B gray-scale camera as a sensor. For the calibration process of the optical system, a white target was illuminated by a point source, and its encoded projections were captured on the sensor. The process was repeated for each spectral band and each shot using the designed encoding. To illustrate a visual comparison of the reconstruction using the proposed approaches in a real noise and real mismatch environment, Fig 12 presents RGB mappings of the reconstructed scene using the proposed approaches and the baseline ℓ_2 method for a gradient-descent and a PnP-FISTA based algorithms, in the first and second block, respectively, from real test-bed measurements. Specifically, the acquired data has a spatial resolution of $M = N = 128$, $L = 13$, and a compression ratio of about 30%. Also, the output of the algorithm was obtained for a different number of iterations to show the faster convergence in the reconstructions of the proposed approaches f_a and f_b. This figure shows that the proposed methods provide more detailed reconstructed images than the baseline approach, employing a reduced number of iterations (before convergence), which corroborates that the proposed approaches are faster than the baseline one. Also, to verify the spectral reconstruction accuracy, the spectral response of two spatial points of the scene was measured with a point spectrometer, to be used as a reference. This spectral response is shown in Fig. 12

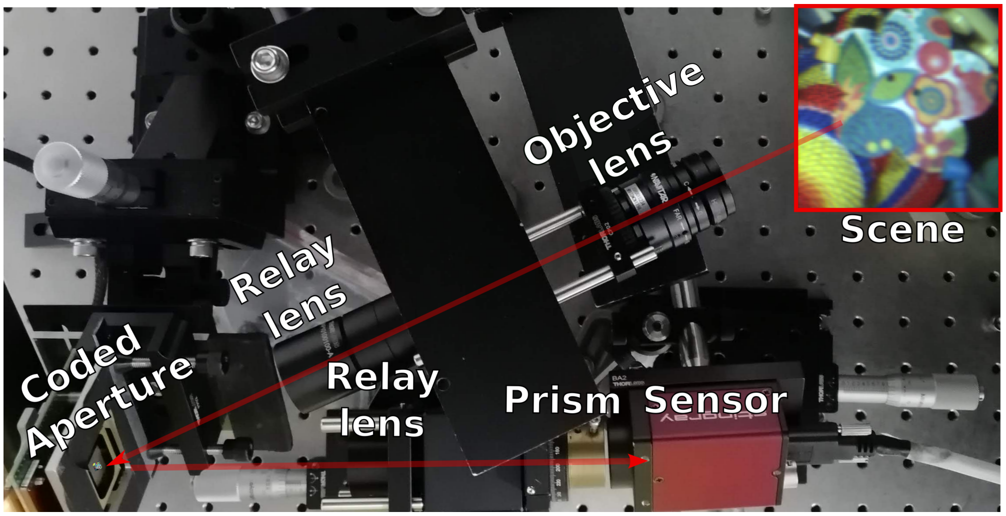

Figura 11. Photography of the CASSI optical system implemented and used to obtain the calibration matrix and the experimental measurements

(last columns), and compared with those attained in the reconstructions, where it is evident that the closest spectral response to the real spectrum was obtained by the proposed approach f_b that reconstructs the image and the mismatch measurement $\mathbf{y}_2$, followed by the proposed approach f_a for a reduced number of iterations. Finally, a less accurate recovered spectrum is obtained with the baseline ℓ_2-based approach, for both cases gradient-descent and PnP-FISTA.

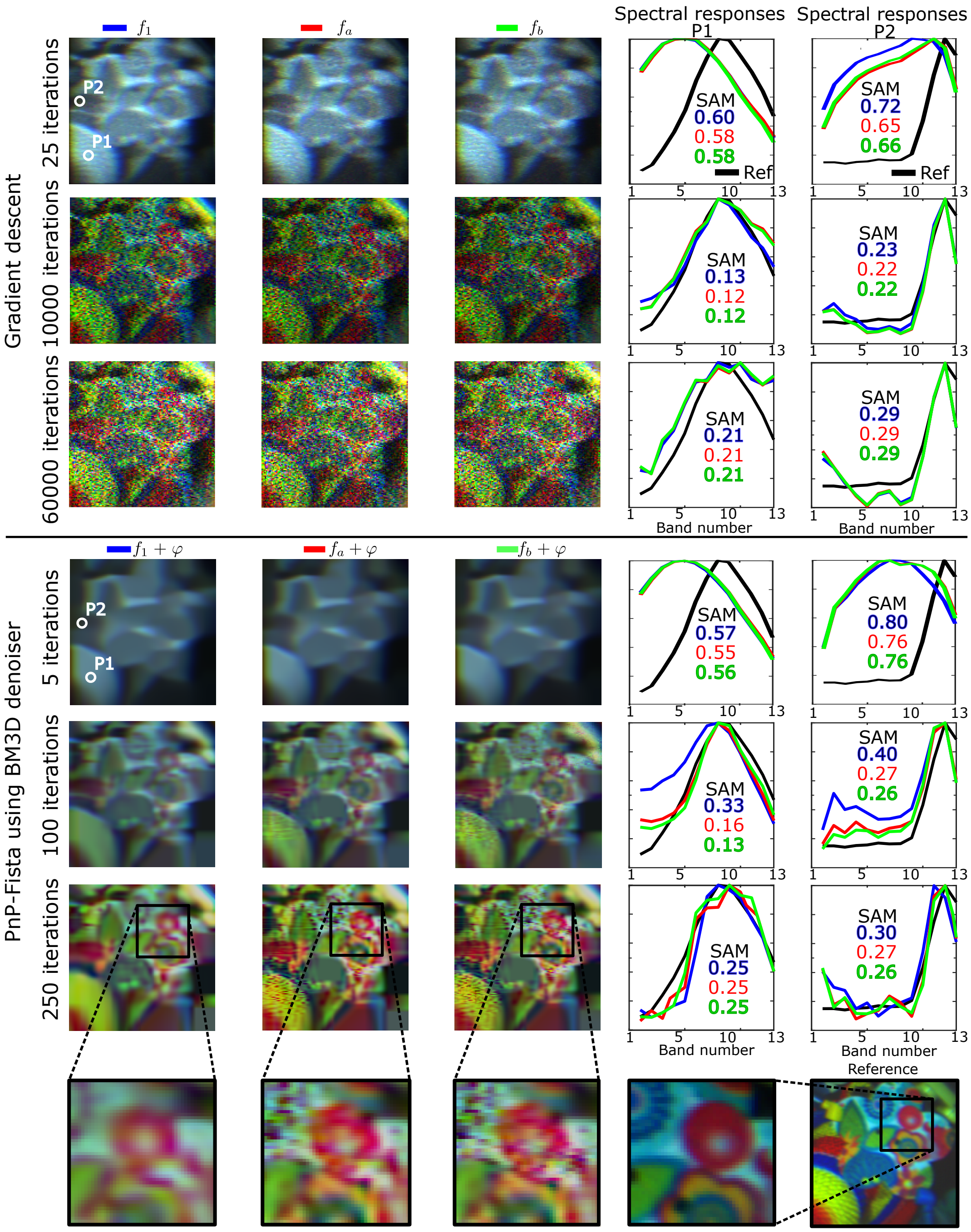

Figura 12. Performance comparison of the proposed approaches with one f_a and two regularizations f_b, compared with baseline f_1 in a real set of measurements for a CASSI optical systems, using a different number of iterations, including the spectral angular mapper (SAM) to compare the spectral responses

6. Misalignment correction in compressive spectral imaging designed system via deep learning strategies

A different way to deal with misalignment correction is using a deep learning approach that correct the measurements, in this developed approach, a neural network $\mathcal{M}$ is trained to minimize

$$\bar{\mathbf{y}}_0 = \arg\min_{\mathcal{P}} \{\mathbf{y}_0 - \mathcal{P}\{\mathbf{y}_1\}\}, \tag{36}$$

remarking that $\mathbf{y}_1$ stand for the measurements acquired with the implemented optical system and $\mathbf{y}_0$ for the desired ideal simulated measurements. To train $\mathcal{P}$ a CASSI optical system was implemented and calibrated in the HDSP optical lab, which includes a side information sensor to capture the ground truth spectral image using a filtered camera strategy (Band by band), this ground truth spectral image is used to obtain the ideal measurements $\mathbf{y}_0$ by simulating the sensing process, which is complemented with public spectral image database Arad et al. (2022). After training the neural network $\mathcal{P}$, using the dataset of pairs $\mathbf{y}_0$ and $\mathbf{y}_1$, different simulations were developed to define the best way to include this information in the reconstruction process.

6.1. Reconstruction approaches

To resolve the inverse problem to recover a scene from compressed measurements $\mathbf{y}_1$, traditionally, the calibrated sensing matrix $\mathbf{H}_1$ is employed in an optimization algorithm to reconstruct the SI, given by

$$\mathbf{x}^* = \arg\min_{\mathbf{x}} \frac{1}{2}||\mathbf{y}_1 - \mathbf{H}_1\mathbf{x}||_2^2 + \lambda||\mathbf{\Psi}(\mathbf{x})||_1, \tag{37}$$

where λ is the regularization constant and $\mathbf{\Psi}$ stands for a transformation basis that promotes a sparse representation of $\mathbf{x}$. For this extension chapter, an optimization gradient-based method is used, specifically the well-known GPSR algorithm was used to reconstruct the vectorized observation form $\mathbf{x}$ of data cube $\mathbf{X}$ solving the inverse problem which uses a regularization parameter λ in the cost function of (37), which consists in minimizing an objective function which includes a quadratic error term combined with a sparseness-in-ducing regularization term Figueiredo et al. (2007).

6.2. Deep learning approach to reduce the implementation effects in the measurements

As shown in Fig. 3, if a better-conditioned sensing matrix $\mathbf{H}_0$ with its measurement $\mathbf{y}_0$ is employed to solve the optimization problem (37) it is possible to obtain a better performance compared with the use of the real calibrated $\mathbf{H}_1$ with the real implemented measurements $\mathbf{y}_1$. then a deep neural network $\mathcal{P}$ that minimize

$$\mathcal{P} = \arg\min_{\mathcal{P}} ||\mathcal{P}\{\mathbf{y}_1\} - \mathbf{y}_0|| = \arg\min_{\mathcal{P}} ||\hat{\mathbf{y}}_0 - \mathbf{y}_0||, \tag{38}$$

where the projection of the real measurements $\mathcal{P}\{\mathbf{y}_1\}$ is renamed as $\hat{\mathbf{y}}_0$, which can be used in (37) jointly with $\mathbf{H}_0$ to obtain a better performance in real scenarios. It is important to remark that this section does not try to obtain the best possible deep learning network but shows that it is possible to increase the performance in the reconstruction task if a deep neural network $\mathcal{P}$ is employed.

6.2.1. K-UNETA: Adapted UNET architecture for K-shots. The correction of measurements shown in (38) is similar to a denoising problem, in this way an autoencoder network is required which has the same input size as the output size. An architecture that accomplished this requirement is shown in Fig. 13, which is based on a classical UNET network adapted for a measurement from the CASSI optical system of $128 \times 140 \times 1$, where it is feasible just for a one-shot CASSI measurements. On the other hand, to generalize the use of this proposed strategy to multishot ($K \geq 1$), it is necessary to include the previous network in a more complex one, this K-shot network K-UNETA is presented in Fig. 14, where each block named UNetA is referred to the one-shot architecture.

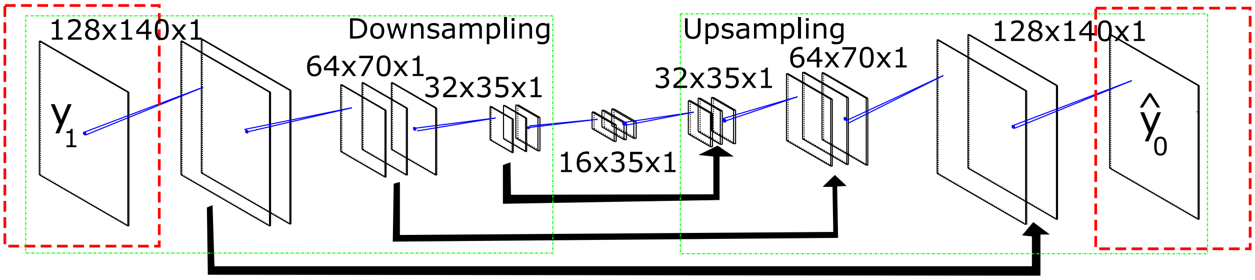

Figura 13. UNET adapted network $\mathcal{P}$ for the one-shot compressive sensing approach, using the traditional forward connections but fixing the downsampling and upsampling scale.

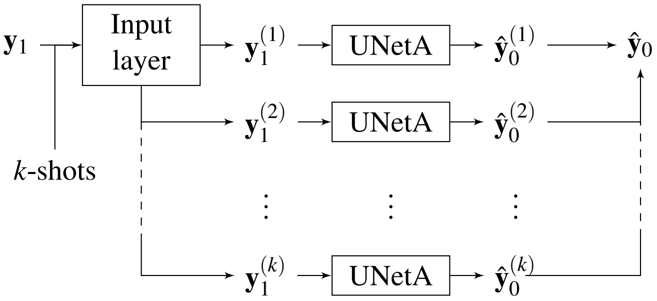

Figura 14. Full $\mathcal{P}$ network for estimation of corrected multi-shot measurement $\hat{\mathbf{y}}_0$ from $\mathbf{y}_1$ in a multi-shot scheme, where $\hat{\mathbf{y}}_1^{(k)}$ refer to the k-th shot.

6.3. Performance analysis estimating the corrected measurements

To test the performance of the proposed methodology, the data set ARAD Arad et al. (2022) was used in training and testing as ideal spectral images, where 450 data cubes are labeled for training and 15 data cubes for validation. The average training time in seconds was 190 per epoch. The data cubes have the size $482 \times 512 \times 31$, thus the spatial data was cropped and the spectral bands sampled in order to obtain a data cube with size $128 \times 128 \times 13$. These changes are aimed to use the sensing matrix designed and real-calibrated in laboratory implementation, which has the dimensions mentioned. The number of shots in the sensing matrix is 8, then the k-UNetA network has 8 threads of data flow. In figures 15 and 16 is shown the performance of the estimation of the ideal $\mathbf{y}_0$ measurements and compared with the real calibrated taken measurements $\mathbf{y}_1$, where it is evident that the estimated $\hat{\mathbf{y}}_0 = \mathcal{P}\{\mathbf{y}_1\}$ is closest to the ideal designed one.

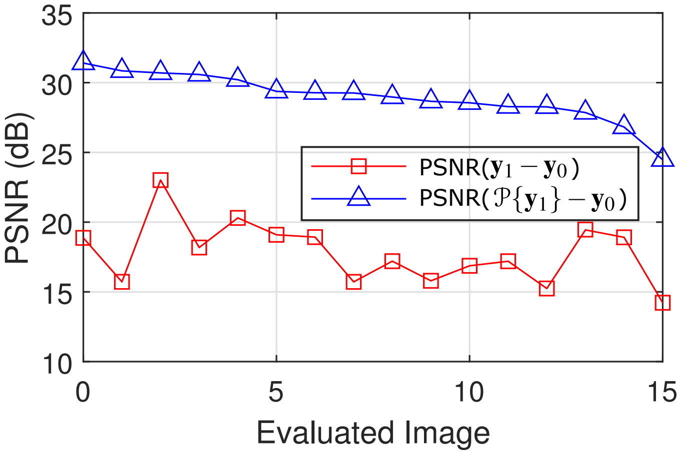

Figura 15. PSNR performance obtained for 15 compressed images for real $\mathbf{y}_1$ and estimated $\hat{\mathbf{y}}_0 = \mathcal{P}\{\mathbf{y}_1\}$ with respect to ideal-expected $\mathbf{y}_0$.

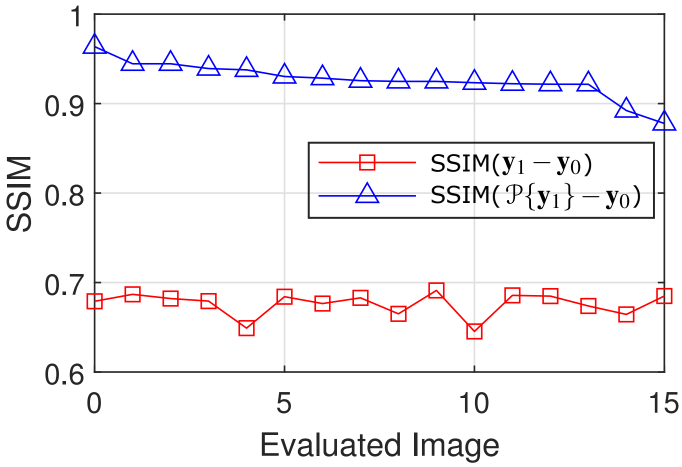

Figura 16. SSIM performance obtained for 15 compressed images for real $\mathbf{y}_1$ and estimated $\hat{\mathbf{y}}_0 = \mathcal{P}\{\mathbf{y}_1\}$ with respect to ideal-expected $\mathbf{y}_0$.

6.4. Performance reconstruction analysis

Taking into account that the deep learning estimated ideal measurement $\hat{\mathbf{y}}_0$ is near to the ideal one $\mathbf{y}_0$ as is shown in section 6.3, this estimated measurement is employed jointly with the designed sensing matrix $\mathbf{H}_0$ to obtain the recovered spectral imaging using (37). A comparison of the performance of employing the real measurements $\mathbf{y}_1$ (traditional case), the simulated ideal measurements $\mathbf{y}_0$ (Desired case) and the estimated $\hat{\mathbf{y}}_0$ (proposed approach) is shown in fig. 17, where the false RGB-colored image shows the improvement of the proposed approach. In figures 18,19 and 20 are presented quantitative comparisons in terms of the PSNR, SSIM, and SAM metrics for a set of 15 images, where is shown that the proposed approach obtains performance as expected between the ideal case and the traditional one.

(a) Data cube.

(b) Ideal $||\mathbf{y}_0 - \mathbf{H}_0\mathbf{x}||_2^2 + \lambda||\mathbf{\Psi}(\mathbf{x})||_1$

(c) Traditional $||\mathbf{y}_1 - \mathbf{H}_1\mathbf{x}||_2^2 + \lambda||\mathbf{\Psi}(\mathbf{x})||_1$

(d) Proposed $||\hat{\mathbf{y}}_0 - \mathbf{H}_0\mathbf{x}||_2^2 + \lambda||\mathbf{\Psi}(\mathbf{x})||_1$

Figura 17. Comparison between ground-truth image, reconstructions for measurements: $\mathbf{y}_0$, $\mathbf{y}_1$, and $\hat{\mathbf{y}}_0$, with PSNR scores of 34.7969, 26.4801, and 28.7086, respectively.

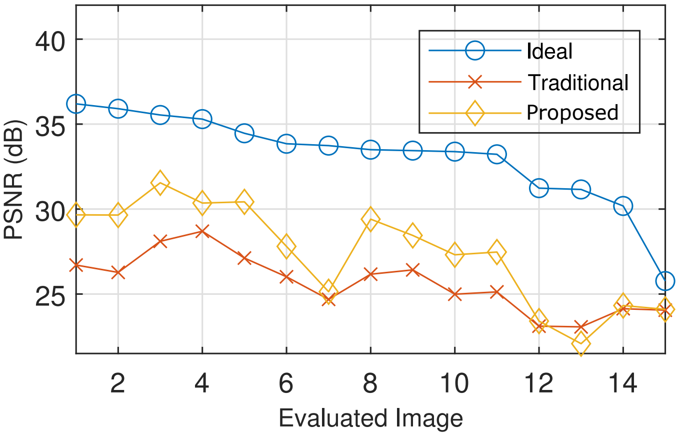

Figura 18. PSNR scores were obtained for 15 images $128 \times 128 \times 13$ using the ideal, traditional, and proposed approach, in all cases 8 shots were employed

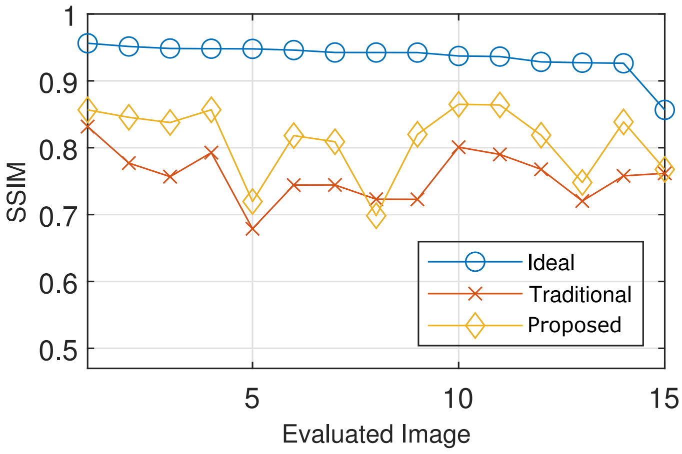

Figura 19. SSIM scores were obtained for 15 images 128 × 128 × 13 using the ideal, traditional, and proposed approach, in all cases 8 shots were employed.

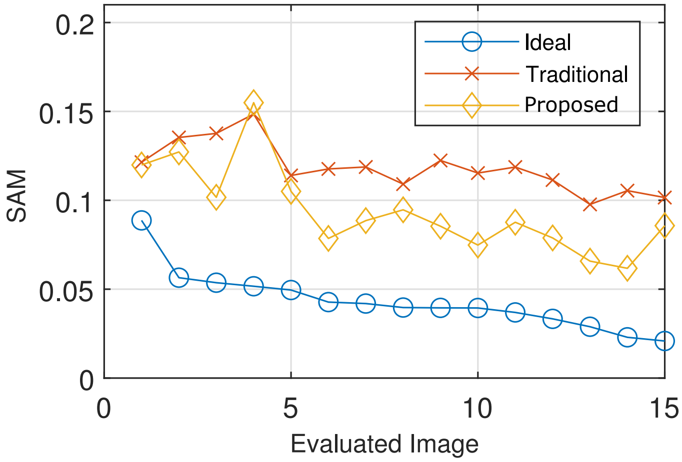

Figura 20. SAM scores were obtained for 15 images 128 × 128 × 13 using the ideal, traditional, and proposed approach, in all cases 8 shots were employed.

7. Conclusions and Future Work

This doctoral thesis studied the problem of loss of performance in spectral image recovery in optimized codified acquisition systems and presents three different approaches to deal with this problem, two of them are based on reinforcement regularization and a last one is based on a deep learning approach, these methods are tested on CASSI and DOE-based optical systems, however, they can be easily extended to any other optical system, in which the sensing process is modeled as linear. It is important to remark that was developed a deep mathematical analysis of the effect, in a gradient-based reconstruction task, caused by the mismatch obtained in the implementation step on linearly modeled compressive spectral imaging systems, and this information was employed to develop the proposed approaches. These proposed approaches show that it is possible to obtain a better performance in implemented-calibrated optimized optical systems than the traditionally obtained employing the calibrated sensing matrix, specifically, this performance can be close to the obtained in simulation using the ideal sensing matrix, remarking that this distortion cannot be modeled a priori to be included in the optimization process. Moreover, the proposed regularization methods provide improvements of up to $2.5dB$ of PSNR in simulations around the 400th iteration and a reduction in up to $50\,\%$ of the required number of iterations to obtain the desired performance quality; and the deep learning-based proposed approach allows the improvements in up to $4dB$ compared with traditional approaches.

Future work includes the implementation of these approaches in other optimized systems for others task as classification or segmentation, and generalizing the approaches to high-dimensional data which can be spectral-video or spectral-depth. Another future work includes the design of robust optimized coding elements that allow the capture of measurements closest to the ideal-modeled and the improvement of the systems model to obtain better-optimized coding elements.

Bibliography

Arad, B., Timofte, R., Yahel, R., Morag, N., Bernat, A., Cai, Y., Lin, J., Lin, Z., Wang, H., Zhang, Y., Pfister, H., Van Gool, L., Liu, S., Li, Y., Feng, C., Lei, L., Li, J., Du, S., Wu, C., Leng, Y., Song, R., Zhang, M., Song, C., Zhao, S., Lang, Z., Wei, W., Zhang, L., Dian, R., Shan, T., Guo, A., Feng, C., Liu, J., Agarla, M., Bianco, S., Buzzelli, M., Celona, L., Schettini, R., He, J., Xiao, Y., Xiao, J., Yuan, Q., Li, J., Zhang, L., Kwon, T., Ryu, D., Bae, H., Yang, H.-H., Chang, H.-E., Huang, Z.-K., Chen, W.-T., Kuo, S.-Y., Chen, J., Li, H., Liu, S., Sabarinathan, S., Uma, K., Bama, B. S., and Roomi, S. M. M. (2022). Ntire 2022 spectral recovery challenge and data set. In *2022 IEEE/CVF Conference on Computer Vision and Pattern Recognition Workshops (CVPRW)*, pages 862–880.

Arce, G. R., Brady, D. J., Carin, L., Arguello, H., and Kittle, D. S. (2014). Compressive coded aperture spectral imaging: An introduction. *IEEE Signal Processing Magazine*, 31(1):105–115.

Arguello, H. and Arce, G. R. (2012). Restricted isometry property in coded aperture compressive spectral imaging. *2012 IEEE Statistical Signal Processing Workshop, SSP 2012*, 0:716–719.

Arguello, H. and Arce, G. R. (2014a). Colored coded aperture design by concentration of measure in compressive spectral imaging. *IEEE Transactions on Image Processing*, 23(4):1896–1908.

Arguello, H. and Arce, G. R. (2014b). Colored coded aperture design by concentration of measure in compressive spectral imaging. *IEEE Transactions on Image Processing*, 23(4):1896–1908.

Arguello, H., Bacca, J., Kariyawasam, H., Vargas, E., Marquez, M., Hettiarachchi, R., Garcia, H., Herath, K., Haputhanthri, U., Ahluwalia, B. S., So, P., Wadduwage, D. N., and Edussooriya, C. U. (2023). Deep optical coding design in computational imaging: A data-driven framework.

Arguello, H., Pinilla, S., Peng, Y., Ikoma, H., Bacca, J., and Wetzstein, G. (2021). Shift-variant color-coded diffractive spectral imaging system. *Optica*, 8(11):1424–1434.

Arguello, H., Rueda, H., Wu, Y., Prather, D. W., and Arce, G. R. (2013). Higher-order computational model for coded aperture spectral imaging. *Applied optics*, 52(10):D12–D21.

Bacca, J., Correa, C. V., and Arguello, H. (2019a). Noniterative hyperspectral image reconstruction from compressive fused measurements. *IEEE Journal of Selected Topics in Applied Earth Observations and Remote Sensing*, 12(4):1231–1239.

Bacca, J., Correa, C. V., Vargas, E., Castillo, S., and Arguello, H. (2019b). Compressive classification from single pixel measurements via deep learning. In *2019 IEEE 29th International Workshop on Machine Learning for Signal Processing (MLSP)*, pages 1–6. IEEE.

Bacca, J., Galvis, L., and Arguello, H. (2020). Coupled deep learning coded aperture design for compressive image classification. *Optics Express*, 28(6):8528–8540.

Bacca, J., Gelvez-Barrera, T., and Arguello, H. (2021). Deep coded aperture design: An end-to-end approach for computational imaging tasks. *IEEE Transactions on Computational Imaging*, 7:1148–1160.

Baek, S.-H., Ikoma, H., Jeon, D. S., Li, Y., Heidrich, W., Wetzstein, G., and Kim, M. H. (2020). End-to-end hyperspectral-depth imaging with learned diffractive optics. *arXiv preprint arXiv:2009.00463*.

Baraniuk, R. and Steeghs, P. (2007). Compressive radar imaging. In *2007 IEEE Radar Conference*, pages 128–133.

Bian, L., Suo, J., Dai, Q., and Chen, F. (2018). Experimental comparison of single-pixel imaging algorithms. *Journal of the Optical Society of America A*, 35(1):78–87.

Calvetti, D. (2007). Preconditioned iterative methods for linear discrete ill-posed problems from a bayesian inversion perspective. *Journal of computational and applied mathematics*, 198(2):378–395.

Candès, E. J. and Wakin, M. B. (2008). An introduction to compressive sampling. *IEEE signal processing magazine*, 25(2):21–30.

Cao, X., Du, H., Tong, X., Dai, Q., and Lin, S. (2011). A prism-mask system for multispectral video acquisition. *IEEE Transactions on Pattern Analysis and Machine Intelligence*, 33(12):2423–2435.

Cao, X., Yue, T., Lin, X., Lin, S., Yuan, X., Dai, Q., Carin, L., and Brady, D. J. (2016). Computational snapshot multispectral cameras: Toward dynamic capture of the spectral world. *IEEE Signal Processing Magazine*, 33(5):95–108.

Chan, S. H., Wang, X., and Elgendy, O. A. (2016). Plug-and-play admm for image restoration: Fixed-point convergence and applications. *IEEE Transactions on Computational Imaging*, 3(1):84–98.

Choi, S., Kim, J., Peng, Y., and Wetzstein, G. (2021). Optimizing image quality for holographic near-eye displays with michelson holography. *Optica*, 8(2):143–146.

Contreras, G., Pabón, J., Garcia, H., Rojas, F., and Arguello, H. (2021). Correction of designed compressive spectral imaging measurements using a deep learning-based method. In *2021 XXIII Symposium on Image, Signal Processing and Artificial Vision (STSIVA)*, pages 1–5.

Correa, C. V., Arguello, H., and Arce, G. R. (2015). Snapshot colored compressive spectral imager. *JOSA A*, 32(10):1754–1763.

Correa, C. V., Arguello, H., and Arce, G. R. (2016). Spatiotemporal blue noise coded aperture design for multi-shot compressive spectral imaging. *JOSA A*, 33(12):2312–2322.

Cuadros, A. P., Arce, G. R., and Arguello, H. (2014). Coded aperture design in compressive x-ray tomography. In *2014 IEEE Global Conference on Signal and Information Processing (GlobalSIP)*, pages 656–659. IEEE.

Dabov, K., Foi, A., Katkovnik, V., and Egiazarian, K. (2007). Image denoising by sparse 3-d transform-domain collaborative filtering. *IEEE Transactions on image processing*, 16(8):2080–2095.

Donoho, D. L. (2006). Compressed sensing. *IEEE Transactions on Information Theory*, 52(4):1289–1306.

Duarte, M. F., Davenport, M., Takhar, D., Laska, J. N., Sun, T. S. T., Kelly, K. F., and Baraniuk, R. G. (2008). Single-Pixel Imaging via Compressive Sampling. *IEEE Signal Processing Magazine*, 25(2):1–19.

Elad, M. (2007). Optimized projections for compressed sensing. *IEEE Transactions on Signal Processing*, 55(12):5695–5702.

Figueiredo, M. A., Nowak, R. D., and Wright, S. J. (2007). Gradient projection for sparse reconstruction: Application to compressed sensing and other inverse problems. *IEEE Journal of selected topics in signal processing*, 1(4):586–597.

GA Shaw, H. K. B. (2003). Spectral Imaging for Remote sensing. *Lincoln Laboratory Journal*, 14(1):3–28.

Galvis, L., Lau, D., Ma, X., Arguello, H., and Arce, G. R. (2017). Coded aperture design in compressive spectral imaging based on side information. *Applied Optics*, 56(22):6332.

Garcia, H., Bacca, J., Wohlberg, B., and Arguello, H. (2023). Calibration reinforcement regularizations for optimized snapshot spectral imaging. *Appl. Opt.*, 62(8):C135–C145.

Garcia, H., Correa, C. V., and Arguello, H. (2020a). Optimized sensing matrix for single pixel multi-resolution compressive spectral imaging. *IEEE Transactions on Image Processing*, 29:4243–4253.

Garcia, H., Espitia, O., and Arguello, H. (2016). Multiresolution spectral imaging by combining different sampling strategies in a compressive imager, mr-cassi. In *2016 XXI Symposium on Signal Processing, Images and Artificial Vision (STSIVA)*, pages 1–6.

Garcia, H., Marquez, M., and Arguello, H. (2020b). Super-resolution in compressive coded imaging systems via l2 â€“ l1 â€“ l2 minimization under a deep learning approach. In *2020 Data Compression Conference (DCC)*, pages 53–62.

Gastal, E. S. L. and Oliveira, M. M. (2011). Domain transform for edge-aware image and video processing. In *ACM SIGGRAPH 2011 Papers*, SIGGRAPH ’11. Association for Computing Machinery.

Green, R. O., Eastwood, M. L., Sarture, C. M., Chrien, T. G., Aronsson, M., Chippendale, B. J., Faust, J. A., Pavri, B. E., Chovit, C. J., Solis, M., Olah, M. R., and Williams, O. (1998). Imaging spectroscopy and the Airborne Visible/Infrared Imaging Spectrometer (AVIRIS). *Remote Sensing of Environment*, 65(3):227–248.

Hinojosa, C., Bacca, J., and Arguello, H. (2018). Coded aperture design for compressive spectral subspace clustering. *IEEE Journal of Selected Topics in Signal Processing*, 12(6):1589–1600.

Hinojosa, C., Sanchez, K., Garcia, H., and Arguello, H. (2022). C-3spcd: coded aperture similarity constrained design forspatio-spectral classification of single-pixel measurements. *Appl. Opt.*, 61(8):E21–E32.

Hong, T. and Zhu, Z. (2018). An efficient method for robust projection matrix design. *Signal Processing*, 143:200–210.

Jácome, R., López, C., Garcia, H., and Arguello, H. (2021). Deep learning-based object classification for spectral images. *Applications of Computational Intelligence*, pages 147–159.

Jagatap, G., Chen, Z., Nayer, S., Hegde, C., and Vaswani, N. (2019). Sample efficient fourier ptychography for structured data. *IEEE Transactions on Computational Imaging*, 6:344–357.

Jeon, D. S., Baek, S.-H., Yi, S., Fu, Q., Dun, X., Heidrich, W., and Kim, M. H. (2019). Compact snapshot hyperspectral imaging with diffracted rotation. *ACM Transactions on Graphics (Proc. SIGGRAPH 2019)*, 38(4):117:1–13.

Jerri, A. J. (1977). The shannon sampling theoremâ€”its various extensions and applications: A tutorial review. *Proceedings of the IEEE*, 65(11):1565–1596.

Kamilov, U. S., Mansour, H., and Wohlberg, B. (2017a). A plug-and-play priors approach for solving nonlinear imaging inverse problems. *IEEE Signal Processing Letters*, 24(12):1872–1876.

Kamilov, U. S., Mansour, H., and Wohlberg, B. (2017b). A plug-and-play priors approach for solving nonlinear imaging inverse problems. *IEEE Signal Processing Letters*, 24(12):1872–1876.

Kellman, M. R., Bostan, E., Repina, N. A., and Waller, L. (2019). Physics-based learned design:

optimized coded-illumination for quantitative phase imaging. *IEEE Transactions on Computational Imaging*, 5(3):344–353.

Landau, H. J. (1967). Sampling, data transmission, and the Nyquist rate. *Proceedings of the IEEE*, 55(10):1701–1706.

Li, C. (1959). Notes on relative fitness of genotypes that forms a geometric progression. *Evolution*, 13(4):564–567.

Lin, X., Liu, Y., Wu, J., and Dai, Q. (2014a). Spatial-spectral encoded compressive hyperspectral imaging. *ACM Trans. Graph.*, 33(6):233:1—-233:11.

Lin, X., Wetzstein, G., Liu, Y., and Dai, Q. (2014b). Dual-Coded Compressive Hyper-Spectral Imaging. *Classical Optics 2014, OSA Technical Digest (online) (Optical Society of America, 2014)*, 39(7):2044–2047.

Lu, G. and Fei, B. (2014). Medical hyperspectral imaging: a review. *Journal of biomedical optics*, 19(1):10901.

Ma, X., Wang, D., Cuadros, A., Mao, T., Zhao, Q., Arce, G. R., and Xu, T. (2020). Conveyor x-ray tomosynthesis imaging with optimized structured sequential illumination. *IEEE Photonics Journal*, 12(5):1–17.

Marwah, K., Wetzstein, G., Bando, Y., and Raskar, R. (2013). Compressive light field photography using overcomplete dictionaries and optimized projections. *ACM Transactions on Graphics (TOG)*, 32(4):1–12.

Mejia, Y. and Arguello, H. (2018). Binary codification design for compressive imaging by uniform sensing. *IEEE Transactions on Image Processing*, 27(12):5775–5786.

Morales-Norato, D., Urrea, S., Garcia, H., Rodriguez-Ferreira, J., Martinez, E., Arguello, H., Silva-Lora, A., Torres, R., Acero, I. F., Hernández, F. L., Cárdenas, L. P., and Rincón, S. (2023). Hyperspectral camera as a compact payload architecture for remote sensing applications. *Appl. Opt.*, 62(8):C88–C98.

Mouroulis, P. and McKerns, M. M. (2000). Pushbroom imaging spectrometer with high spectroscopic data fidelity: experimental demonstration. *Optical Engineering*, 39(3):808–816.

Roman-Gonzalez, A. and Vargas-Cuentas, N. I. (2014). Análisis de imágenes hiperespectrales Hyperspectral images analysis. *Revista Ingenieria & Desarrollo*, 35:14–17.

Rueda, H., Arguello, H., and Arce, G. R. (2015). Colored Coded Aperture Compressive Spectral Imaging : Design and Experimentation. *2015 IEEE Global Conference on Signal and Information Processing (GlobalSIP)*, 1:601–604.

Rueda-Chacon, H., Florez-Ospina, J. F., Lau, D. L., and Arce, G. R. (2019). Snapshot compressive tof+ spectral imaging via optimized color-coded apertures. *IEEE transactions on pattern analysis and machine intelligence*, 42(10):2346–2360.

Saad, Y. (2003). *Iterative methods for sparse linear systems*. SIAM.

Sitzmann, V., Diamond, S., Peng, Y., Dun, X., Boyd, S., Heidrich, W., Heide, F., and Wetzstein, G.

(2018). End-to-end optimization of optics and image processing for achromatic extended depth of field and super-resolution imaging. *ACM Transactions on Graphics (TOG)*, 37(4):1–13.

Song, G., Sun, Y., Liu, J., Wang, Z., and Kamilov, U. S. (2020). A new recurrent plug-and-play prior based on the multiple self-similarity network. *IEEE Signal Processing Letters*, 27:451–455.

Stellman, C. M., Olchowski, F. M., and Michalowicz, J. V. (2001). WAR HORSE (wide-area reconnaissance: hyperspectral overhead real-time surveillance experiment). In *Proc. SPIE*, volume 4379, pages 339–346.

Takhar, D., Laska, J. N., Wakin, M. B., Duarte, M. F., Baron, D., Sarvotham, S., Kelly, K. F., and Baraniuk, R. G. (2006). A new compressive imaging camera architecture using optical-domain compression. *Proceedings of SPIE*, 6065:606509–606510.

Tian, L., Li, X., Ramchandran, K., and Waller, L. (2014). Multiplexed coded illumination for fourier ptychography with an led array microscope. *Biomedical optics express*, 5(7):2376–2389.

Venkatakrishnan, S. V., Bouman, C. A., and Wohlberg, B. (2013). Plug-and-play priors for model based reconstruction. In *2013 IEEE Global Conference on Signal and Information Processing*, pages 945–948. IEEE.

Wagadarikar, A., John, R., Willett, R., and Brady, D. (2008a). Single disperser design for coded aperture snapshot spectral imaging. *Appl. Opt.*, 47(10):B44—-B51.

Wagadarikar, A., John, R., Willett, R., and Brady, D. (2008b). Single disperser design for coded aperture snapshot spectral imaging. *Applied optics*, 47(10):44–51.

Wang, L., Zhang, T., Fu, Y., and Huang, H. (2018). Hyperreconnet: Joint coded aperture optimization and image reconstruction for compressive hyperspectral imaging. *IEEE Transactions on Image Processing*, 28(5):2257–2270.

Xie, M., Sun, Y., Liu, J., Wohlberg, B., and Kamilov, U. S. (2020). Joint reconstruction and calibration using regularization by denoising. *arXiv preprint arXiv:2011.13391*.

Yeh, L.-H., Tian, L., and Waller, L. (2017). Structured illumination microscopy with unknown patterns and a statistical prior. *Biomedical optics express*, 8(2):695–711.

Zhang, G., Jiao, S., Xu, X., and Wang, L. (2010). Compressed sensing and reconstruction with bernoulli matrices. In *The 2010 IEEE International Conference on Information and Automation*, pages 455–460. IEEE.